

CHEMISTRY IN INFRARED DARK CLOUD CLUMPS: A MOLECULAR LINE SURVEY AT 3 mm

PATRICIO SANHUEZA¹, JAMES M. JACKSON¹, JONATHAN B. FOSTER¹, GUIDO GARAY², ANDREA SILVA³, SUSANNA C. FINN¹

Submitted: February 18, 2012; Accepted: June 24, 2012

ABSTRACT

We have observed 37 Infrared Dark Clouds (IRDCs), containing a total of 159 clumps, in high-density molecular tracers at 3 mm using the 22-meter ATNF Mopra Telescope located in Australia. After determining kinematic distances, we eliminated clumps that are not located in IRDCs and clumps with a separation between them of less than one Mopra beam. Our final sample consists of 92 IRDC clumps. The most commonly detected molecular lines are (detection rates higher than 8%): N₂H⁺, HNC, HN¹³C, HCO⁺, H¹³CO⁺, HCN, C₂H, HC₃N, HNCO, and SiO. We investigate the behavior of the different molecular tracers and look for chemical variations as a function of an evolutionary sequence based on *Spitzer* IRAC and MIPS emission. We find that the molecular tracers behave differently through the evolutionary sequence and some of them can be used to yield useful relative age information. The presence of HNC and N₂H⁺ lines do not depend on the star formation activity. On the other hand, HC₃N, HNCO, and SiO are predominantly detected in later stages of evolution. Optical depth calculations show that in IRDC clumps the N₂H⁺ line is optically thin, the C₂H line is moderately optically thick, and HNC and HCO⁺ are optically thick. The HCN hyperfine transitions are blended, and, in addition, show self-absorbed line profiles and extended wing emission. These factors combined prevent the use of HCN hyperfine transitions for the calculation of physical parameters. Total column densities of the different molecules, except C₂H, increase with the evolutionary stage of the clumps. Molecular abundances increase with the evolutionary stage for N₂H⁺ and HCO⁺. The N₂H⁺/HCO⁺ and N₂H⁺/HNC abundance ratios act as chemical clocks, increasing with the evolution of the clumps.

Keywords: Astrochemistry — ISM: clouds — ISM: molecules — ISM: abundances — stars: formation

1. INTRODUCTION

Although far less common than low-mass stars, massive stars play a key role in the evolution of the energetics and chemistry of molecular clouds and galaxies. However, the formation of high-mass stars is far less clear than their low-mass counterparts for several reasons. Massive stars are rare and evolve quickly. In addition, the regions that host their early stages of formation are difficult to observe due to high dust extinction, and, with a few exceptions, are located at large distances ($\gtrsim 3$ kpc). For this reason, most of the research on massive star formation has been based on observations of regions with current star formation (e.g., “hot cores,” H II regions), which were initially easier to detect in surveys and to follow up in detail. In contrast, objects in the earlier “prestellar” or “starless” stage have been much harder to find and, in consequence, this stage still remains poorly understood.

About a decade ago, however, the regions containing the earliest stages of massive star formation were identified. Galactic plane surveys revealed thousands of dark patches obscuring the bright mid-infrared background (*ISO*, Perault et al. 1996; *MSX*, Egan et al. 1998, Simon et al. 2006a; *Spitzer*, Peretto & Fuller 2009, Kim et al. 2010). These dark silhouettes were associated with molecular and dust emission, indicating they con-

sist of dense molecular gas. Such objects were called Infrared Dark Clouds (IRDCs). The first studies characterizing them suggested that they were cold (<25 K), massive ($\sim 10^2$ – $10^4 M_{\odot}$), and dense ($\gtrsim 10^5$ cm⁻³) molecular clouds with high column densities ($\gtrsim 10^{23}$ cm⁻²) (Carey et al. 1998, 2000). They also correspond to the densest clouds embedded within giant molecular clouds (Simon et al. 2006b).

More recent studies on IRDC clumps,⁴ using dust continuum emission, show that they have typical masses of $\sim 120 M_{\odot}$ and sizes ~ 0.5 pc (Rathborne et al. 2006). Spectral energy distributions (SEDs) of several IRDC clumps reveal dust temperatures that range between 16 and 52 K, and luminosities that range from ~ 10 – $10^5 L_{\odot}$ (Rathborne et al. 2010). Temperatures derived using NH₃ observations are lower than dust temperatures and range from ~ 10 – 20 K (Pillai et al. 2006; Sakai et al. 2008; Devine et al. 2011; Ragan et al. 2011). Star formation activity in IRDC clumps can be inferred from high temperatures and high luminosities as well as the presence of UC H II regions (Battersby et al. 2010), hot cores (Rathborne et al. 2008), embedded 24 μ m sources (Chambers et al. 2009), molecular outflows (Beuther & Sridharan 2007; Sanhueza et al. 2010), and maser emission (Wang et al. 2006; Chambers et al. 2009). The high masses, densities, and column densities of the IRDC clumps, as well as the aforementioned sig-

¹ Institute for Astrophysical Research, Boston University, Boston, MA 02215, USA

² Departamento de Astronomía, Universidad de Chile, Casilla 36-D, Santiago, Chile

³ Harvard-Smithsonian Center for Astrophysics, 60 Garden Street, Cambridge, MA 02138, USA

⁴ Throughout this paper, we use the term “clump” to refer to a dense object within an IRDC with a size of the order ~ 1 pc and a mass $\sim 10^2$ – $10^3 M_{\odot}$. We use the term “core” to describe a compact, dense object within a clump with a size $\lesssim 0.1$ pc and a mass $\lesssim 50 M_{\odot}$.

natures of star formation in them, indicate that IRDCs are currently forming massive stars. In addition, IRDCs harbor numerous candidates for the most elusive earliest phase of high-mass star formation, the “prestellar” or “starless” phase (Chambers et al. 2009; Rathborne et al. 2010; Rygl et al. 2010; Vasyunina et al. 2011; Pillai et al. 2011; Devine et al. 2011). Due to the characteristics of IRDCs and the large variety of evolutionary stages that they harbor, it has been suggested that they are the natal sites of all massive stars and stellar clusters (Rathborne et al. 2006, 2010).

With the aim of characterizing the different evolutionary stages of clumps found in IRDCs, Chambers et al. (2009) proposed an evolutionary sequence in which “quiescent” clumps evolve into “intermediate”, “active”, and “red” clumps. This evolutionary scheme is based on the *Spitzer*/IRAC 3-8 μm colors and the presence or absence of *Spitzer*/MIPS 24 μm point-source emission. A clump is called “quiescent” if it contains no IR-*Spitzer* emission (it is IR-dark); “intermediate” if it contains either an enhanced 4.5 μm emission, the so-called “green fuzzies” (also known as Extended Green Objects (EGOs); Cyganowski et al. 2008), or a 24 μm source, but not both; “active” if it is associated with a green fuzzy and an embedded 24 μm source; and “red” if it is associated with bright 8 μm emission, which likely corresponds to an H II region. Quiescent clumps are the best candidates to be in the “prestellar” or “starless” phase, and the massive quiescent clumps are the places where it is most probable that high-mass stars are in their earliest stages of evolution. An additional category is “blue,” which describes objects with bright 3.6 μm emission that are predominantly unextincted stars.

Although several properties of IRDCs have been determined in the last few years, there is still one that remains poorly explored, their chemistry. What is the chemistry in IRDC clumps? Are the evolutionary stages defined by Chambers et al. (2009) chemically distinguishable? Presently, only a few studies have focused on this subject (Sakai et al. 2008, 2010, 2012; Vasyunina et al. 2011; Miettinen et al. 2011; Chen et al. 2011).

In this paper, we report initial results from a program aimed at better understanding the chemical evolution of IRDC clumps, carrying out a multi-line survey at 3 mm. We observed several molecular lines simultaneously, which facilitates comparison between different lines by eliminating or reducing observational errors arising from uncertainties in telescope pointing and calibrations. The main goals of this project are to investigate the behavior of the different molecular tracers and look for observable changes in the chemistry as a function of the evolutionary stages proposed by Chambers et al. (2009).

2. OBSERVATIONS

2.1. The Sample

We made single-pointing observations of molecular lines at 3 mm using the ATNF Mopra 22 m telescope⁵ located in Australia. The source list comprises 37 IRDCs, containing a total of 159 clumps. This is a sub-sample of the 38 IRDCs and 190 clumps identified

by Rathborne et al. (2006) using 1.2 mm dust continuum emission at 11'' angular resolution. The threshold limit for a molecular line to be considered as a detection was defined at the 3σ level, where σ is the rms noise in antenna temperature (T_{rms} ; see Table 1). The clumps G015.31 MM4, G027.75 MM5, G028.37 MM5, and G030.57 MM4 present no molecular line emission above the 3σ detection level; consequently, they are not included in any analysis throughout this work. We excluded 17 clumps that show signs of star formation at IR wavelengths (*Spitzer*) and are located at a different distance than the rest of the clumps within an IRDC (see Section 3.4 for more details). These clumps belong to a different molecular cloud that is situated in the line of sight. Since the Mopra telescope beam size (38'') is sometimes comparable to the separation between clumps within the same IRDC, $\sim 30\%$ of the sources are contaminated by emission from another adjacent clump. To ensure that the observed emission is attributable solely to a single clump, and not a neighboring clump, each source with an angular separation smaller than the Mopra beam size from its nearest neighbor was excluded. Furthermore, blue clumps are not included in any analysis because they are likely unextincted stars. Therefore, this work will focus on the remaining 92 IRDC clumps unless stated otherwise. Chambers et al. (2009) and Rathborne et al. (2010) classified the initial sample of 190 IRDC clumps using a combination of *Spitzer*/IRAC colors and the presence or absence of compact 24 μm emission. Their classifications differ in the method of estimating the 24 μm flux measurements. Chambers et al. (2009) used aperture photometry, and Rathborne et al. (2010) fitted a Gaussian to the radial profile of the emission. Due to this difference, in a few cases 24 μm emission is detected for a particular source using one method, but not the other. In this work, to avoid ambiguities, if a clump presents 24 μm emission from either of the two methods, a 24 μm compact source will be assigned to the clump.

Table 2 summarizes information for all 159 IRDC clumps: names, coordinates, velocities, distances, dust temperatures, *Spitzer* classification, and if the source is an IRDC and if it is used in the present work.

2.2. Observing Parameters

The observations were carried out during 2008 July–August and 2010 September. They were performed with the 3 mm Monolithic Microwave Integrated Circuits (MMIC) receiver and the Mopra spectrometer (MOPS)⁶ in the “broad-band” mode, resulting in a total bandwidth of 8.3 GHz split over four overlapping sub-bands of 2.2 GHz. Each sub-band has 2×8096 channels (1×8096 per each polarization) with a channel resolution of 0.27 MHz. The velocity resolution was $\sim 0.90 \text{ km s}^{-1}$ per channel. Both polarizations were observed and averaged to improve the signal to noise ratio. The observed frequencies range between 85.540 and 93.840 GHz. This frequency range allowed us to observe 15 molecular lines simultaneously (see Table 1). The system temperatures ranged between 165 and 265 K. Typical rms noise values (T_{rms})

⁵ The Mopra telescope is part of the Australia Telescope National Facility (ATNF) which is funded by the Commonwealth of Australia for operation as a National Facility managed by CSIRO.

⁶ The University of New South Wales Digital Filter Bank used for the observations with the Mopra Telescope was provided with support from the Australian Research Council.

Table 1
Summary of Observed Molecular Lines

Molecule	Transition	Rest Frequency (GHz)	E_u/k (K)	n_{crit} (cm^{-3})	IF	T_{rms} (K)
NH ₂ D	$J_{K_a, K_c} = 1_{1,1} - 1_{0,1}$	85.926260	20.68	4×10^6	IF3	0.044
SO	$N_J = 2_2 - 1_1$	86.093983	19.31	2×10^5	IF3	0.044
H ¹³ CN	$J = 1 - 0, F = 1 - 1$	86.338735	4.14	2×10^6	IF3	0.044
	$J = 1 - 0, F = 2 - 1$	86.340167	4.14	2×10^6	IF3	0.044
	$J = 1 - 0, F = 0 - 1$	86.342256	4.14	2×10^6	IF3	0.044
H ¹³ CO ⁺	$J = 1 - 0$	86.754330	4.16	2×10^5	IF3	0.044
SiO	$J = 2 - 1$	86.846998	6.25	2×10^6	IF3	0.044
HN ¹³ C	$J = 1 - 0$	87.090859	4.18	3×10^5	IF3	0.044
C ₂ H	$N = 1 - 0, J = 3/2 - 1/2, F = 2 - 1$	87.316925	4.19	2×10^{5a}	IF3	0.044
	$N = 1 - 0, J = 3/2 - 1/2, F = 1 - 0$	87.328624	4.19	2×10^{5a}	IF3	0.044
	$N = 1 - 0, J = 1/2 - 1/2, F = 1 - 1$	87.402004	4.19	2×10^{5a}	IF3	0.044
	$N = 1 - 0, J = 1/2 - 1/2, F = 0 - 1$	87.407165	4.19	2×10^{5a}	IF3	0.044
HNCO	$J_{K_a, K_b} = 4_{0,4} - 3_{0,3}$	87.925252	10.55	1×10^6	IF2	0.048
HCN	$J = 1 - 0, F = 1 - 1$	88.630416	4.25	3×10^6	IF2	0.048
	$J = 1 - 0, F = 2 - 1$	88.631847	4.25	3×10^6	IF2	0.048
	$J = 1 - 0, F = 0 - 1$	88.633936	4.25	3×10^6	IF2	0.048
HCO ⁺	$J = 1 - 0$	89.188526	4.28	2×10^5	IF2	0.048
HNC	$J = 1 - 0$	90.663574	4.35	3×10^5	IF1	0.042
HC ₃ N	$J = 10 - 9$	90.978989	24.01	5×10^5	IF1	0.042
CH ₃ CN	$J_K = 5_1 - 4_1$	91.985316	20.39	4×10^5	IF0	0.042
	$J_K = 5_0 - 4_0$	91.987089	13.24	5×10^5	IF0	0.042
¹³ CS	$J = 2 - 1$	92.494303	6.00	3×10^5	IF0	0.042
N ₂ H ⁺	$J = 1 - 0, F_1 = 1 - 1, F = 2 - 2$	93.171913	4.47	3×10^5	IF0	0.042
	$J = 1 - 0, F_1 = 2 - 1, F = 3 - 2$	93.173772	4.47	3×10^5	IF0	0.042
	$J = 1 - 0, F_1 = 0 - 1, F = 1 - 2$	93.176261	4.47	3×10^5	IF0	0.042

Note. — The critical density was calculated as $n_{\text{crit}} = A_{ul}/\gamma_{ul}$, where A_{ul} is the Einstein coefficient and γ_{ul} is the collisional rate. Values of A_{ul} and γ_{ul} at 20 K (50 K for SO) were obtained for most of the molecules from the Leiden Atomic and Molecular Database (LAMDA) (Schöier et al. 2005). Values of A_{ul} and γ_{ul} at 25 K for NH₂D were obtained from Machin & Roueff (2006).

^a Critical density adopted from Lo et al. (2009).

for each molecular line are shown in Table 1. The on-source integration time per object was ~ 3 minutes. The angular resolution of Mopra telescope is $38''$ and its main beam efficiency is 0.5 at 90 GHz.⁷ All the observations were performed in position-switching mode with the off-position shifted from the target source by 1° in Galactic latitude away from the Galactic midplane. The telescope pointing was checked by observing nearby SiO masers every ~ 1 hr, and was maintained to be better than $5''$. The uncertainty in the line intensity varies with the frequency from 9% at 88 GHz to 25% at 93 GHz (Jonathan Foster, private communication). The initial spectral processing was done using the ATNF Spectral Analysis Package (ASAP) software.⁸ The observed molecular lines, transitions, rest frequencies, upper energy levels, critical densities, sub-bands, and typical T_{rms} are listed in Table 1. The T_{rms} for each source is given in Table 3.

3. RESULTS

3.1. Line Parameters

For each molecular transition, the line center velocity, line width and intensity of the line were determined from Gaussian fits. Molecular lines that show hyperfine structure (N₂H⁺ and C₂H) were fitted using a multi-Gaussian function, with a fixed frequency separation between the transitions. The Gaussian fit procedure was carried

out in IDL using the MPFITFUN package (Markwardt 2009). Occasionally, two velocity components were detected in a source. We define the main component, i.e., the component associated with the IRDC clump, as the velocity component detected in the high-density tracers (e.g., N₂H⁺ and/or H¹³CO⁺). The secondary velocity component typically corresponds to lower-density gas located in line of sight and they were not used in this work. When two velocity components have emission from high-density tracers, the brightest was used as the main component. The Gaussian fit parameters of the main velocity component for all sources where emission was detected (155) are summarized in Table 3. No Gaussian fits were carried out for two distinct velocity components with separations less than 3 km s^{-1} or for self-absorbed profiles.

3.2. Spectra and Detection Rates

Figure 1 presents the detection rates, at the 3σ detection level, of the 10 most frequently detected molecular species toward the IRDC clumps. For the N₂H⁺ and C₂H lines, we show the most often detected transitions: $JF_1F = 123 \rightarrow 012$ for N₂H⁺ and $NJF = 1\frac{3}{2}2 \rightarrow 0\frac{1}{2}1$ for C₂H. Because the HCN transitions are blended, and in addition, exhibit self-absorbed profiles and wing emission, the multi-Gaussian fit to the hyperfine structure was not reliable. The HCN detection rate was obtained by inspecting the spectrum for each source by eye, instead of comparing the intensity of the Gaussian fit with the T_{rms} . The CH₃CN, ¹³CS, H¹³CN, SO,

⁷ See more details about Mopra telescope, receivers, and backends at <http://www.narrabri.atnf.csiro.au/mopra/obsinfo.html>

⁸ <http://www.atnf.csiro.au/computing/software/>

and NH₂D lines were detected in fewer than 8 clumps; therefore, their detection rates are not presented in Figure 1. The molecular lines most often detected were HNC $J = 1 \rightarrow 0$ and N₂H⁺ $JF_1F = 123 \rightarrow 012$ with 90 (98%) and 89 (97%) detections, respectively. On the

other hand, the molecular line shown in Figure 1 least often detected was the SiO $J = 2 \rightarrow 1$ with 8 (9%) detections. Detection rates for all detected molecular transitions are given in Table 4. Uncertainties presented in Figure 1 and Table 4 were determined assuming Poisson noise.

Table 2
Clumps Properties.

IRDC Name	Clump Number	Coordinates		V_{lsr}^a (km s ⁻¹)	D (kpc)	T_{dust} (K)	Class. ^b	Comment ^e
		α (J2000)	δ (J2000)					
G015.05+00.07	MM1	18:17:50.4	-15:53:38	25.2	2.8	23.5	Q	IRDC
G015.05+00.07	MM2	18:17:40.0	-15:48:55	29.9	3.1	30.5	R	IRDC
G015.05+00.07	MM3	18:17:42.4	-15:47:03	28.4	3.0	23.7	Q	IRDC
G015.05+00.07	MM4	18:17:32.0	-15:46:35	28.0	3.0	30.5	Q	IRDC
G015.05+00.07	MM5	18:17:40.2	-15:49:47	29.9	3.1	31.0	Q	IRDC
G015.31-00.16	MM1	18:18:56.4	-15:45:00	17.0 ^c	1.9 ^c	...	R	Non-IRDC
G015.31-00.16	MM2	18:18:50.4	-15:43:19	30.9	3.2	23.0	I	IRDC
G015.31-00.16	MM3	18:18:45.3	-15:41:58	31.1	3.2	23.7	Q	IRDC
G015.31-00.16	MM4	18:18:48.0	-15:44:22	31.1 ^d	1.9 ^d	...	Q	No Detection
G015.31-00.16	MM5	18:18:49.1	-15:42:47	31.2 ^c	3.2 ^c	28.0	Q	IRDC
G018.82-00.28	MM1	18:25:56.1	-12:42:48	41.7	3.5	...	I	Non-IRDC
G018.82-00.28	MM2	18:26:23.4	-12:39:37	63.1	4.7	38.0	R	IRDC
G018.82-00.28	MM3	18:25:52.6	-12:44:37	44.8	3.7	34.0	A	IRDC
G018.82-00.28	MM4	18:26:15.5	-12:41:32	65.5	4.8	17.0	I	IRDC
G018.82-00.28	MM6	18:26:18.4	-12:41:15	65.8	4.8	23.7	Q	IRDC
G019.27+00.07	MM1	18:25:58.5	-12:03:59	26.7	2.4	...	B	Bright Blue
G019.27+00.07	MM2	18:25:52.6	-12:04:48	26.7	2.4	30.0	A	IRDC
G022.35+00.41	MM1	18:30:24.4	-09:10:34	52.7	3.9	20.0	A	IRDC
G022.35+00.41	MM2	18:30:24.2	-09:12:44	59.9 ^c	4.2 ^c	44.0	R	IRDC
G023.60+00.00	MM1	18:34:11.6	-08:19:06	106.5	7.0	...	A	Non-IRDC
G023.60+00.00	MM2	18:34:21.1	-08:18:07	53.7	3.9	...	A	Blended
G023.60+00.00	MM3	18:34:10.0	-08:18:28	105.8	6.9	...	R	Non-IRDC
G023.60+00.00	MM4	18:34:23.0	-08:18:21	53.6	3.9	...	R	Blended
G023.60+00.00	MM5	18:34:09.5	-08:18:00	104.8	6.8	...	A	Non-IRDC
G023.60+00.00	MM7	18:34:21.1	-08:17:11	54.0	3.9	44.0	I	IRDC
G023.60+00.00	MM9	18:34:22.5	-08:16:04	54.3	3.9	32.5	Q	IRDC
G024.08+00.04	MM1	18:34:57.0	-07:43:26	114.1	7.8	...	R	Non-IRDC
G024.08+00.04	MM2	18:34:51.1	-07:45:32	114.1	7.8	29.0	Q	IRDC
G024.08+00.04	MM3	18:35:02.2	-07:45:25	51.6	3.7	29.0	Q	IRDC
G024.08+00.04	MM4	18:35:02.6	-07:45:56	52.2	3.7	30.0	Q	IRDC
G024.33+00.11	MM1	18:35:07.9	-07:35:04	114.1	7.8	...	R	Blended
G024.33+00.11	MM2	18:35:34.5	-07:37:28	118.2	7.7	32.5	I	IRDC
G024.33+00.11	MM3	18:35:27.9	-07:36:18	117.6	7.7	31.5	R	IRDC
G024.33+00.11	MM4	18:35:19.4	-07:37:17	115.0	7.8	31.0	Q	IRDC
G024.33+00.11	MM5	18:35:33.8	-07:36:42	117.2	7.7	32.0	I	IRDC
G024.33+00.11	MM6	18:35:07.7	-07:34:33	114.3	7.7	...	I	Blended
G024.33+00.11	MM7	18:35:09.8	-07:39:48	99.6	6.3	23.7	Q	IRDC
G024.33+00.11	MM8	18:35:23.4	-07:37:21	113.8	7.8	31.5	Q	IRDC
G024.33+00.11	MM9	18:35:26.5	-07:36:56	119.2	7.7	52.0	R	IRDC
G024.33+00.11	MM11	18:35:05.1	-07:35:58	113.3	7.8	26.0	Q	IRDC
G024.60+00.08	MM1	18:35:41.1	-07:18:30	53.4	3.8	...	A	Blended
G024.60+00.08	MM2	18:35:39.3	-07:18:51	115.2	7.7	23.0	I	IRDC
G024.60+00.08	MM3	18:35:40.2	-07:18:37	53.8	3.8	...	I	Blended
G024.60+00.08	MM4	18:35:35.7	-07:18:09	53.2	3.8	...	Q	Blended
G025.04-00.20	MM1	18:38:10.2	-07:02:34	64.0	4.3	...	A	Blended
G025.04-00.20	MM2	18:38:17.7	-07:02:51	63.5	4.3	28.0	I	IRDC
G025.04-00.20	MM3	18:38:10.2	-07:02:44	63.7	4.3	...	Q	Blended
G025.04-00.20	MM4	18:38:13.7	-07:03:12	63.8	4.3	29.5	I	IRDC
G025.04-00.20	MM5	18:38:12.0	-07:02:44	63.9	4.3	...	Q	Blended
G027.75+00.16	MM1	18:41:19.9	-04:32:20	78.3	5.0	...	A	Blended
G027.75+00.16	MM2	18:41:33.0	-04:33:44	51.4	3.5	24.0	Q	IRDC
G027.75+00.16	MM3	18:41:16.8	-04:31:55	78.7	5.0	...	I	Blended
G027.75+00.16	MM5	18:41:23.6	-04:30:42	79.1 ^d	4.8 ^d	...	Q	No Detection
G027.94-00.47	MM1	18:44:03.6	-04:38:00	45.4	3.1	44.0	R	IRDC
G027.97-00.42	MM1	18:43:52.8	-04:36:13	44.6	3.1	...	A	Blended
G027.97-00.42	MM2	18:43:58.0	-04:34:24	19.9	1.5	...	R	Non-IRDC
G027.97-00.42	MM3	18:43:54.9	-04:36:08	45.9	3.2	...	Q	Blended
G028.04-00.46	MM1	18:44:08.5	-04:33:22	45.8	3.2	38.0	A	IRDC
G028.08+00.07	MM1	18:42:20.3	-04:16:42	81.4	5.2	22.0	I	IRDC
G028.10-00.45	MM1	18:44:12.9	-04:29:45	47.1	3.2	...	Q	Blended
G028.10-00.45	MM2	18:44:14.3	-04:29:48	46.9	3.2	...	Q	Blended
G028.23-00.19	MM1	18:43:30.7	-04:13:12	80.0	5.1	22.0	Q	IRDC
G028.23-00.19	MM2	18:43:29.0	-04:12:16	80.8	5.1	...	I	Blended
G028.23-00.19	MM3	18:43:30.0	-04:12:33	80.2	5.1	...	Q	Blended

Table 2 — *Continued*

IRDC Name	Clump Number	Coordinates		V_{lsr}^a (km s ⁻¹)	D (kpc)	T_{dust} (K)	Class. ^b	Comment ^e
		α (J2000)	δ (J2000)					
G028.28-00.34	MM1	18:44:15.0	-04:17:54	48.7	3.3	...	R	Blended
G028.28-00.34	MM2	18:44:21.3	-04:17:37	84.9	5.6	...	R	Non-IRDC
G028.28-00.34	MM3	18:44:13.4	-04:18:05	49.7	3.4	...	R	Blended
G028.28-00.34	MM4	18:44:11.4	-04:17:22	48.8	3.4	34.5	A	IRDC
G028.37+00.07	MM1	18:42:52.1	-03:59:45	78.1	5.0	33.0	A	IRDC
G028.37+00.07	MM2	18:42:37.6	-04:02:05	80.8	5.1	39.0	I	IRDC
G028.37+00.07	MM3	18:43:03.1	-04:06:24	99.8	6.4	...	R	Non-IRDC
G028.37+00.07	MM4	18:42:50.7	-04:03:15	79.3	5.0	32.0	A	IRDC
G028.37+00.07	MM5	18:42:26.8	-04:01:30	78.6 ^d	4.8 ^d	...	R	No Detection
G028.37+00.07	MM6	18:42:49.0	-04:02:23	80.0	5.1	23.0	A	IRDC
G028.37+00.07	MM7	18:42:56.3	-04:07:31	46.6	3.2	...	R	Non-IRDC
G028.37+00.07	MM8	18:42:49.7	-04:09:54	107.2	7.5	...	R	Non-IRDC
G028.37+00.07	MM9	18:42:46.7	-04:04:08	79.4	5.0	24.5	Q	IRDC
G028.37+00.07	MM10	18:42:54.0	-04:02:30	79.1	5.0	...	A	Blended
G028.37+00.07	MM11	18:42:42.7	-04:01:44	80.9	5.1	36.0	A	IRDC
G028.37+00.07	MM12	18:43:09.9	-04:06:52	34.8	2.5	23.7	Q	IRDC
G028.37+00.07	MM13	18:42:41.8	-03:57:08	77.5	4.9	30.4	I	IRDC
G028.53-00.25	MM1	18:44:18.0	-03:59:34	86.8	5.5	...	Q	Blended
G028.53-00.25	MM2	18:44:15.7	-03:59:41	85.6	5.4	...	A	Blended
G028.53-00.25	MM3	18:44:16.0	-04:00:48	86.4	5.5	22.0	Q	IRDC
G028.53-00.25	MM4	18:44:18.6	-04:00:05	86.3	5.4	...	I	Blended
G028.53-00.25	MM5	18:44:17.0	-04:02:04	87.0	5.7	30.0	I	IRDC
G028.53-00.25	MM6	18:44:17.8	-04:00:05	86.4	5.5	...	Q	Blended
G028.53-00.25	MM7	18:44:23.7	-04:02:09	88.6	5.6	23.0	Q	IRDC
G028.53-00.25	MM8	18:44:22.0	-04:01:35	88.6	5.6	28.0	Q	IRDC
G028.53-00.25	MM9	18:44:19.3	-03:58:05	87.1	5.7	28.0	I	IRDC
G028.53-00.25	MM10	18:44:18.5	-03:58:43	86.8	5.5	30.0	Q	IRDC
G028.67+00.13	MM1	18:43:03.1	-03:41:41	84.3 ^c	5.3 ^c	40.0	R	IRDC
G028.67+00.13	MM2	18:43:07.1	-03:44:01	79.2	5.0	23.0	I	IRDC
G028.67+00.13	MM3	18:42:58.2	-03:48:20	103.9	6.9	...	A	Non-IRDC
G030.14-00.06	MM1	18:46:35.7	-02:31:03	86.8	5.5	27.0	A	IRDC
G030.57-00.23	MM1	18:48:00.0	-02:07:20	90.7	5.8	34.5	A	IRDC
G030.57-00.23	MM2	18:47:58.7	-02:15:20	111.3	7.3	...	R	Non-IRDC
G030.57-00.23	MM3	18:47:54.5	-02:11:15	95.9	6.3	23.0	I	IRDC
G030.57-00.23	MM4	18:48:01.8	-02:12:35	86.2 ^d	5.2 ^d	...	Q	No Detection
G030.97-00.14	MM1	18:48:21.6	-01:48:27	77.8	5.0	37.0	A	IRDC
G031.02-00.10	MM1	18:48:09.9	-01:45:17	76.9	4.9	...	B	Bright Blue
G031.97+00.07	MM1	18:49:36.3	-00:45:45	95.0	6.5	...	A	Blended
G031.97+00.07	MM2	18:49:36.0	-00:46:16	94.6	6.5	...	Q	Blended
G031.97+00.07	MM3	18:49:32.3	-00:47:02	94.1	6.4	...	Q	Blended
G031.97+00.07	MM4	18:49:33.0	-00:47:33	95.5	6.6	...	I	Blended
G031.97+00.07	MM5	18:49:21.9	-00:50:35	96.5	6.8	35.0	I	IRDC
G031.97+00.07	MM6	18:49:35.0	-00:46:44	94.8	6.5	...	Q	Blended
G031.97+00.07	MM7	18:49:28.4	-00:48:54	93.9	6.4	27.0	Q	IRDC
G031.97+00.07	MM8	18:49:29.1	-00:48:12	94.5	6.4	47.0	A	IRDC
G033.69-00.01	MM1	18:52:58.8	00:42:37	105.7	7.1	25.0	R	IRDC
G033.69-00.01	MM2	18:52:49.9	00:37:57	104.8	7.1	41.0	R	IRDC
G033.69-00.01	MM3	18:52:50.8	00:36:43	103.1	7.1	43.0	R	IRDC
G033.69-00.01	MM4	18:52:56.4	00:43:08	106.2	7.1	28.0	A	IRDC
G033.69-00.01	MM5	18:52:47.8	00:36:47	105.5	7.1	37.0	A	IRDC
G033.69-00.01	MM11	18:52:56.2	00:41:48	107.0	7.1	25.0	Q	IRDC
G034.43+00.24	MM1	18:53:18.0	01:25:24	57.9	3.8	38.0	A	IRDC
G034.43+00.24	MM2	18:53:18.6	01:24:40	57.4	3.8	...	R	Blended
G034.43+00.24	MM3	18:53:20.4	01:28:23	59.4	3.9	...	A	Blended
G034.43+00.24	MM4	18:53:19.0	01:24:08	57.6	3.8	...	A	Blended
G034.43+00.24	MM5	18:53:19.8	01:23:30	58.0	3.8	23.0	A	IRDC
G034.43+00.24	MM6	18:53:18.6	01:27:48	58.6	3.8	...	I	Blended
G034.43+00.24	MM7	18:53:18.3	01:27:13	58.1	3.8	29.5	I	IRDC
G034.43+00.24	MM8	18:53:16.4	01:26:20	57.2	3.7	43.0	A	IRDC
G034.43+00.24	MM9	18:53:18.4	01:28:14	58.7	3.8	...	Q	Blended
G034.77-00.55	MM1	18:56:48.2	01:18:47	44.2	2.9	40.4	R	IRDC
G034.77-00.55	MM2	18:56:50.3	01:23:16	42.0	2.8	...	Q	Blended
G034.77-00.55	MM3	18:56:44.7	01:20:42	43.1	2.8	30.4	I	IRDC
G034.77-00.55	MM4	18:56:48.9	01:23:34	42.1	2.8	...	Q	Blended
G035.39-00.33	MM1	18:56:41.2	02:09:52	64.3	4.2	...	R	Non-IRDC
G035.39-00.33	MM2	18:56:59.2	02:04:53	54.0	3.5	...	A	Non-IRDC
G035.39-00.33	MM3	18:57:05.3	02:06:29	55.3	3.6	...	R	Non-IRDC
G035.39-00.33	MM4	18:57:06.7	02:08:23	45.3	3.0	...	A	Blended
G035.39-00.33	MM5	18:57:08.8	02:08:09	90.1	6.9	...	Q	Blended
G035.39-00.33	MM6	18:57:08.4	02:09:09	45.5	3.0	...	A	Blended
G035.39-00.33	MM7	18:57:08.1	02:10:50	45.9	3.0	34.0	A	IRDC
G035.59-00.24	MM1	18:57:02.3	02:17:04	50.4	3.3	36.0	R	IRDC
G035.59-00.24	MM2	18:57:07.4	02:16:14	45.3	3.0	24.0	A	IRDC
G035.59-00.24	MM3	18:57:11.6	02:16:08	45.0	3.0	30.5	A	IRDC

Table 2 — *Continued*

IRDC Name	Clump Number	Coordinates		V_{lsr}^a (km s ⁻¹)	D (kpc)	T_{dust} (K)	Class. ^b	Comment ^e
		α (J2000)	δ (J2000)					
G036.67-00.11	MM1	18:58:39.6	03:16:16	53.5	3.5	20.0	Q	IRDC
G036.67-00.11	MM2	18:58:35.6	03:15:06	53.3	3.5	16.0	Q	IRDC
G038.95-00.47	MM1	19:04:07.4	05:08:48	42.4	2.8	16.0	I	IRDC
G038.95-00.47	MM2	19:04:03.4	05:07:56	42.1	2.8	40.0	R	IRDC
G038.95-00.47	MM3	19:04:07.4	05:09:44	42.4	2.8	28.0	I	IRDC
G038.95-00.47	MM4	19:04:00.6	05:09:06	42.1	2.8	43.0	A	IRDC
G048.65-00.29	MM2	19:21:47.6	13:49:22	33.8	2.5	...	Q	Blended
G053.11+00.05	MM1	19:29:17.2	17:56:21	21.8	1.8	38.0	R	IRDC
G053.11+00.05	MM2	19:29:20.2	17:57:06	22.9	1.9	36.0	A	IRDC
G053.11+00.05	MM3	19:29:00.6	17:55:11	2.6	0.5	...	R	Non-IRDC
G053.11+00.05	MM4	19:29:20.4	17:55:04	21.7	1.8	40.0	A	IRDC
G053.11+00.05	MM5	19:29:26.3	17:54:53	21.7	1.8	45.0	R	IRDC
G053.25+00.04	MM1	19:29:39.0	18:01:42	24.9	2.0	35.0	I	IRDC
G053.25+00.04	MM2	19:29:33.0	18:01:00	24.3	2.0	...	B	Bright Blue
G053.25+00.04	MM3	19:29:44.0	17:58:47	23.5	1.9	35.0	I	IRDC
G053.25+00.04	MM4	19:29:34.5	18:01:39	24.5	2.0	37.0	A	IRDC
G053.25+00.04	MM5	19:29:39.4	17:58:40	23.7	1.9	35.0	I	IRDC
G053.25+00.04	MM6	19:29:31.5	17:59:50	23.8	1.9	46.0	A	IRDC
G053.31+00.00	MM1	19:29:50.0	18:05:07	22.0	1.8	...	I	Blended
G053.31+00.00	MM2	19:29:42.1	18:03:57	25.2	2.0	25.0	Q	IRDC
G053.31+00.00	MM3	19:29:49.7	18:04:39	22.2	1.8	...	I	Blended

Note. — Units of right ascension are hours, minutes and seconds, and units of declination are degrees, arcminutes and arcseconds.

^a Velocity from the N_2H^+ $JF_1F = 123 \rightarrow 012$ transition.

^b Denotes the classification based on *Spitzer*/IRAC colors and the presence or absence of *Spitzer*/MIPS 24 μm emission.

^c Velocity and distance determined from the HCO^+ line.

^d Velocity and distance from Rathborne et al. (2010).

^e IRDC: the clump is located in an IRDC (the 92 sources of this study).

Non-IRDC: the clump is not associated with an IRDC. Non-Detection: no molecular line was detected in this survey. Bright Blue: objects with bright 3.6 μm emission that are predominantly unextincted stars. Blended: the angular separation between two sources is less than one Mopra beam.

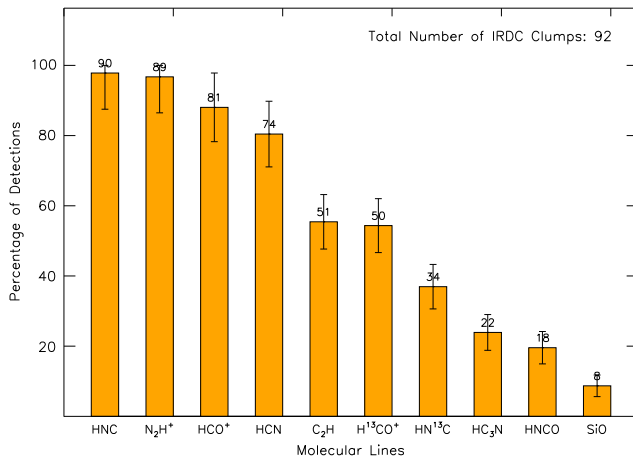


Figure 1. Detection rates of the observed molecular lines toward IRDC clumps. The N_2H^+ and C_2H detection rates correspond to those of the $JF_1F = 123 - 012$ and $NJF = 1 \frac{3}{2} 2 \rightarrow 0 \frac{1}{2} 1$ transitions, respectively. Error bars are the Poisson noise (i.e., the root square of the number of detections). Values on bars are number of detections for a given molecule.

Figures 2, 3, 4, and 5 show representative examples

of spectra for one clump of each proposed evolutionary stage: the quiescent G028.53 MM3, the intermediate G025.04 MM4, the active G034.43 MM1, and the red G034.77 MM1, respectively. The *Spitzer*/IRAC image of the corresponding host IRDC is also displayed in each figure. The active clump G034.43 MM1 (Figure 4) exhibits more molecular line emission than the quiescent clump G028.53 MM3 (Figure 2). This pattern is typical through the sample. It is expected that when star-forming clumps evolve to later stages, they should display a rich molecular spectrum with numerous lines because the proto-stars heat their environment releasing more complex molecules from dust mantles into the gas phase; in contrast, in earlier stages clumps should show a sparse spectrum with a smaller number of detectable molecular lines because many molecules are frozen out onto grain surfaces. However, one must be aware that although the analysis of detection rates may reflect the chemical composition of clumps to some extent, it does not give unambiguous conclusions because detection rates may just show the dependence on H_2 column density. A more definitive conclusion must be drawn from molecular abundances (see Sections 4.2 and 4.4). Figure 6 presents histograms which compare the number of detected molecular transitions for each group. More molecular transitions are detected toward clumps that show signs of star formation. The median number of detections for quiescent clumps is 6 molecular transitions. On the other hand, intermediate and active clumps have a median of 7 and 9 detected molecular transitions, respectively. To quantify the differences between quiescent and active clumps, we have calculated the probability that these two distributions in Figure 6 arise from the same underlying population using the Kolmogorov–Smirnov (K–S) test. The K–S test is a more robust method for measuring the similarity between two distributions than the comparison of the median and/or mean values. Through this paper, we will mention that the difference between two distributions is statistically significant when the K–S test gives a percentage lower than 5%. The probability that the

quiescent and active clumps are derived from the same parent population is 0.1%.

Table 3
N₂H⁺ $JF_1F = 123 \rightarrow 012$ Gaussian Parameters.

IRDC Name	Clump Number	T_{rms} (K)	T_{A} (K)	V_{lsr} (km s ⁻¹)	ΔV (km s ⁻¹)
G015.05+00.07	MM1	0.04	0.38 ± 0.03	25.21 ± 0.10	3.18 ± 0.31
G015.05+00.07	MM2	0.04	0.19 ± 0.03	29.87 ± 0.20	3.64 ± 0.62
G015.05+00.07	MM3	0.04	0.18 ± 0.03	28.41 ± 0.21	2.50 ± 0.54
G015.05+00.07	MM4	0.04	0.44 ± 0.03	27.95 ± 0.08	2.37 ± 0.21
G015.05+00.07	MM5	0.05	0.25 ± 0.05	29.93 ± 0.16	2.03 ± 0.46

Note. — This table is available in its entirety in a machine-readable form in the online journal. A portion is shown here for guidance regarding its form and content.

The median for red clumps is 6 detections. Red clumps (which show bright 8 μm emission) likely correspond to embedded H II regions, a more evolved stage than active clumps. Despite this, they have the same median value as quiescent clumps. In the histogram, red clumps seem to have a bimodal distribution with a first population of 8 clumps showing a low number of detected molecular transitions (left side of the histogram) and a second one of 7 clumps presenting a higher number (right side of the histogram). Moreover, we note that the first population only has one maser detection, and the second population has five (Chambers et al. 2009). These two different populations for red clumps may be the result of the evolutionary state of the H II region. We expect to detect more molecular lines from an early H II region compared to a late H II region because, since the early H II region has not had as much time to ionize the surrounding gas, it should have more molecular gas near the central heating star(s). The molecular spectrum of a late stage H II region, where much of the gas has been ionized, should be more sparse.

The active clump G034.43 MM1 (Figure 4) exhibits a spectrum of a “hot core.” It shows emission in the HNC, HC₃N, and CH₃CN lines, which require high densities and temperatures for excitation ($n_{\text{crit}} \geq 5 \times 10^5 \text{ cm}^{-3}$ and $E_u/k > 10 \text{ K}$), and depend on the release of their parent molecules from dust grains to be formed. In addition, it shows SiO emission, which is usually associated with molecular outflows since SiO abundance is highly enhanced by shocks (e.g., Schilke et al. 1997; Caselli et al. 1997). In contrast, the quiescent clump G028.53 MM3 (Figure 2) presents no emission of HNC, HC₃N, CH₃CN, and SiO over the 3σ limit. The intermediate clump G025.04 MM4 (Figure 3) seems to be in an intermediate chemical state, only exhibiting one high-excitation line (HNC). To carry out a more comprehensive study of the full sample of IRDC clumps, we have split the histogram of detection rates (Figure 1) into four new histograms. In Figure 7 the detection rates for each proposed evolutionary sequence are presented. The detection rates for the quiescent clumps are displayed in every panel for comparison. Quiescent, intermediate, active, and red clumps have 28, 23, 26, and 15 members, respectively. From the histograms in Figure 7, it is seen that the HNC $J = 1 \rightarrow 0$, N₂H⁺ $JF_1F = 123 \rightarrow 012$, and HCO⁺ $J = 1 \rightarrow 0$ lines are present in almost ev-

ery IRDC clump at any evolutionary stage. Red and active clumps have a high detection rate ($\sim 95\%$) for the HCN $J = 1 \rightarrow 0$ line, comparable with the three lines previously mentioned, while in less evolved clumps this value is lower ($\sim 69\%$). There is a high enhancement in the detection of the brightest C₂H line, transition $NJF = 1 \frac{3}{2} 2 \rightarrow 0 \frac{1}{2} 1$, toward active and intermediate clumps with respect to quiescent clumps. The percentages of detection for the H¹³CO⁺ $J = 1 \rightarrow 0$ line are roughly the same for red, intermediate, and quiescent clumps; however, the value for active clumps increases by $\sim 30\%$ with respect to the other three evolutionary stages. The detection rates of the HN¹³C $J = 1 \rightarrow 0$ line show no significant difference between red and intermediate clumps with respect to quiescent clumps; on the other hand, the value for active clumps increases by $\sim 30\%$. The most remarkable difference between detection rates for the different evolutionary stages is found for the HC₃N $J = 10 \rightarrow 9$ line. The detection of this line is significantly high for all stages with IR signs of star formation. HC₃N is only detected in one quiescent source, and the difference between the detection rate in active and quiescent clumps is $\sim 40\%$. While the HNC $J_{K_a, K_b} = 4_{0,4} \rightarrow 3_{0,3}$ line is only detected twice (7%) in quiescent clumps, active and intermediate clumps have a HNC $J_{K_a, K_b} = 4_{0,4} \rightarrow 3_{0,3}$ detection rate of $\sim 27\%$, indicating that this line is also observed more often toward clumps with current star formation. In the quiescent, intermediate, and red clumps, SiO $J = 2 - 1$ emission was rarely detected. In active clumps, the detection rate of SiO reaches the 19%.

3.3. Velocity Widths

The widths of molecular lines give information about the turbulence of clumps. Although we cannot rule out that clumps have organized velocity structures, such as rotation, in this paper we will assume that turbulence dominates the widths of the lines. To investigate if turbulence is different in clumps with and without signs of star formation, we made histograms of the number distributions of full width at half maximum line widths (ΔV) for the four evolutionary stages using the three most commonly detected lines: N₂H⁺, HCO⁺, and HNC. In Figure 8, the number distributions of N₂H⁺ ΔV for each evolutionary sequence is presented. The range of line widths varies between 1.6 and 4.6 km s⁻¹ for the full sample of IRDC clumps. The median values for quiescent, intermediate, active, and red clumps are 2.7, 2.8, 3.0, and 3.4 km s⁻¹, respectively. Using the K-S test, we calculated

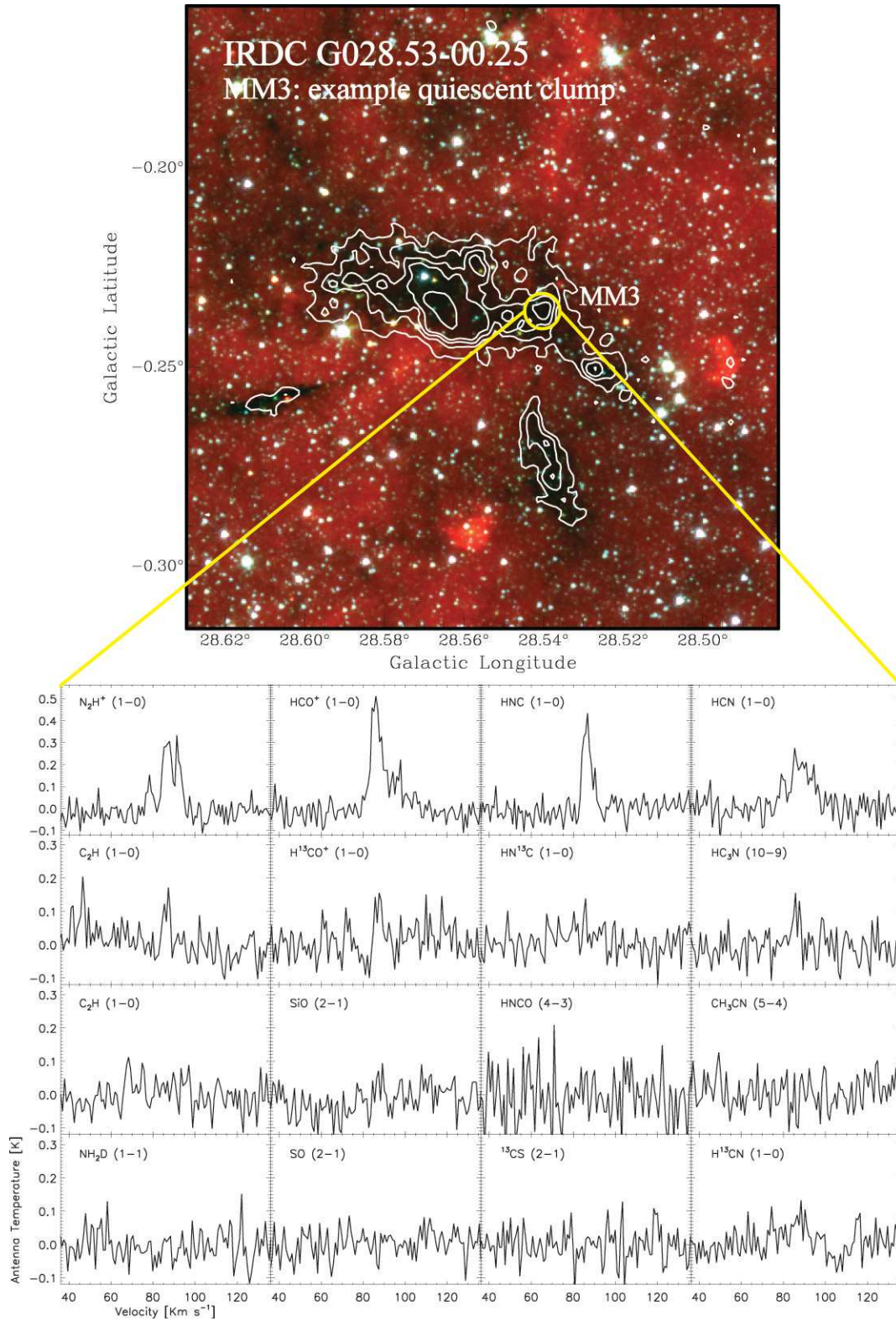


Figure 2. Quiescent clump example. *Top:* IRAC 3-color (3.6 μm in blue, 4.5 μm in green and 8.0 μm in red) image of the IRDC G028.53-00.25 overlaid with IRAM 1.2 mm continuum emission from Rathborne et al. (2006). *Bottom:* Molecular spectra of the quiescent MM3 clump. Quiescent clumps contain none IR emission. The circle shows the telescope beam size and marks the position of the observed clump.

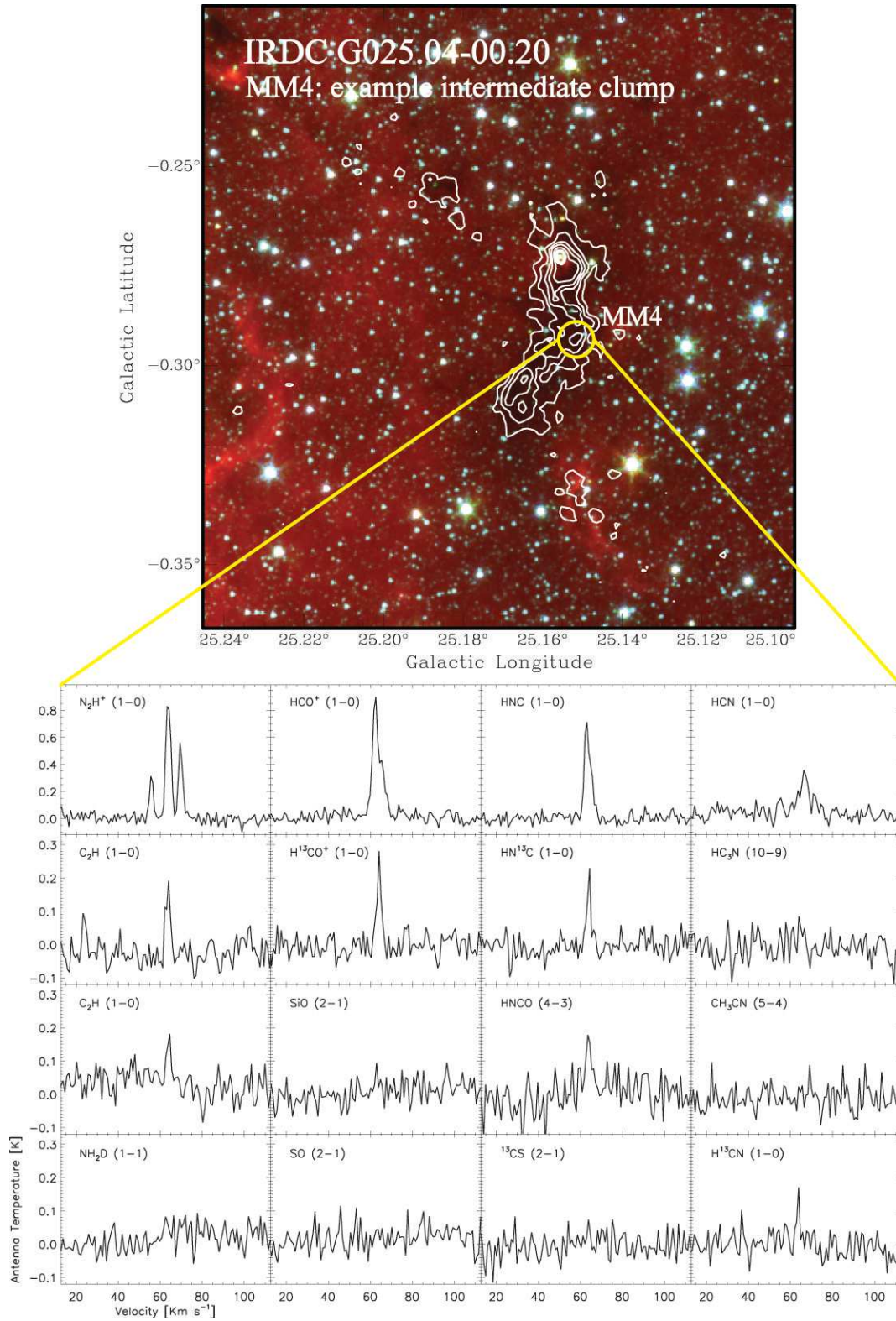


Figure 3. Intermediate clump example. *Top:* IRAC 3-color (3.6 μm in blue, 4.5 μm in green and 8.0 μm in red) image of the IRDC G025.04-00.20 overlaid with IRAM 1.2 mm continuum emission from Rathborne et al. (2006). *Bottom:* Molecular spectra of the intermediate MM4 clump. Intermediate clumps contain either a green fuzzy or a 24 μm source, but not both. The circle shows the telescope beam size and marks the position of the observed clump.

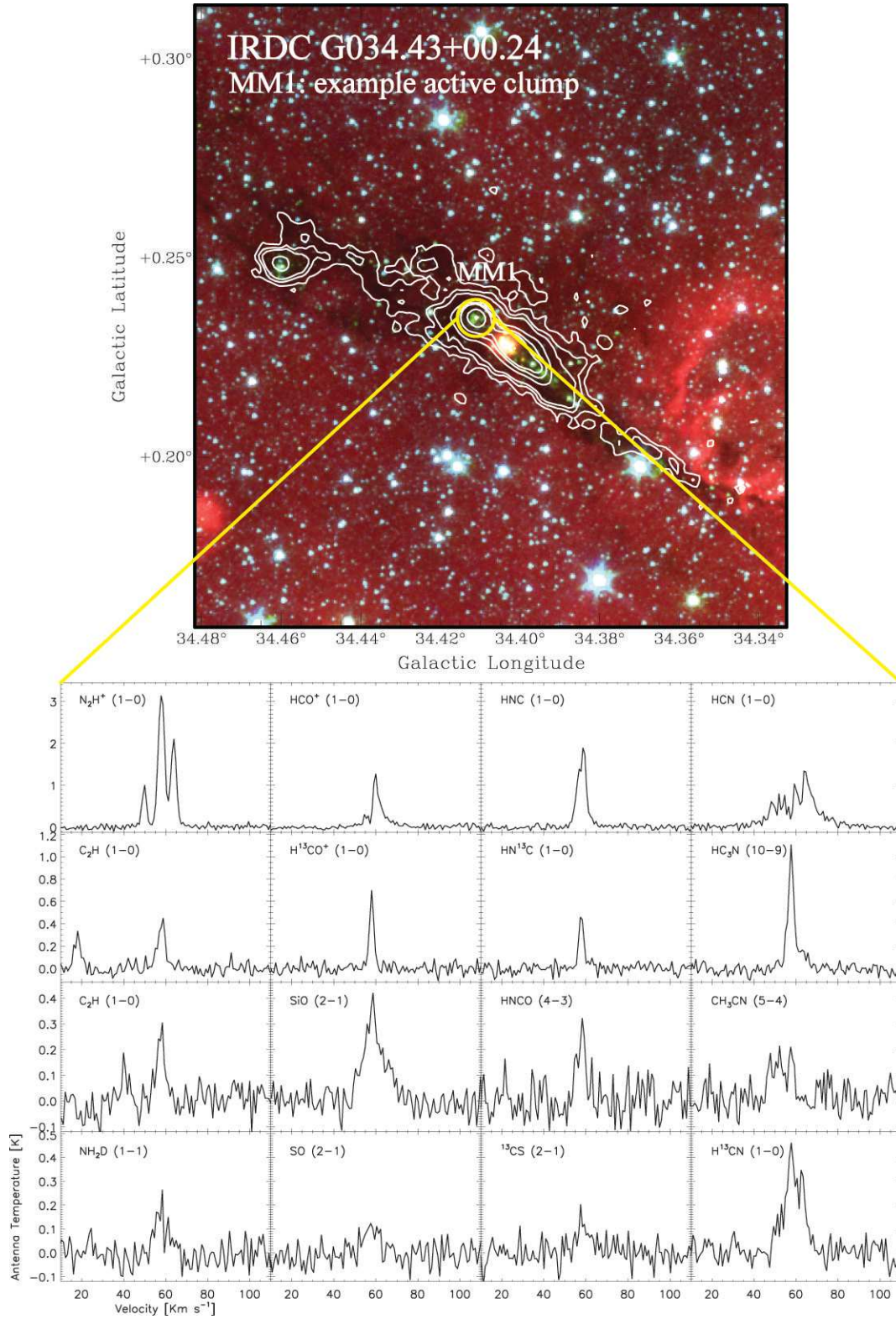


Figure 4. Active clump example. *Top:* IRAC 3-color (3.6 μm in blue, 4.5 μm in green and 8.0 μm in red) image of the IRDC G034.43+00.24 overlaid with IRAM 1.2 mm continuum emission from Rathborne et al. (2006). *Bottom:* Molecular spectra of the active MM1 clump. Active clumps are associated with enhanced 4.5 μm emission, the so-called green fuzzies, and an embedded 24 μm source. The circle shows the telescope beam size and marks the position of the observed clump.

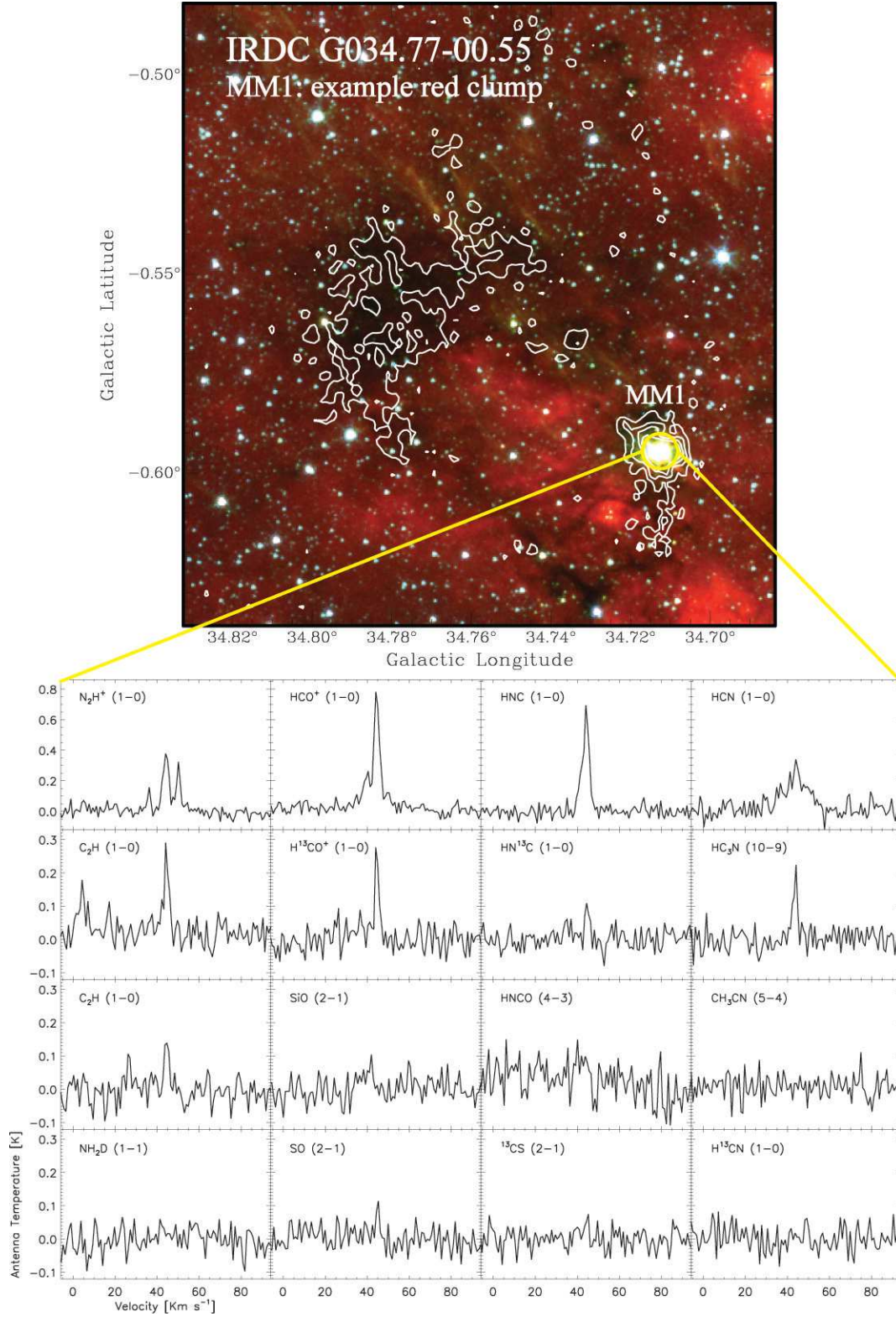


Figure 5. Red clump example. *Top:* IRAC 3-color (3.6 μm in blue, 4.5 μm in green and 8.0 μm in red) image of the IRDC G034.77-00.55 overlaid with IRAM 1.2 mm continuum emission from Rathborne et al. (2006). *Bottom:* Molecular spectra of the red MM1 clump. Red clumps are associated with bright 8 μm emission. The circle shows the telescope beam size and marks the position of the observed clump.

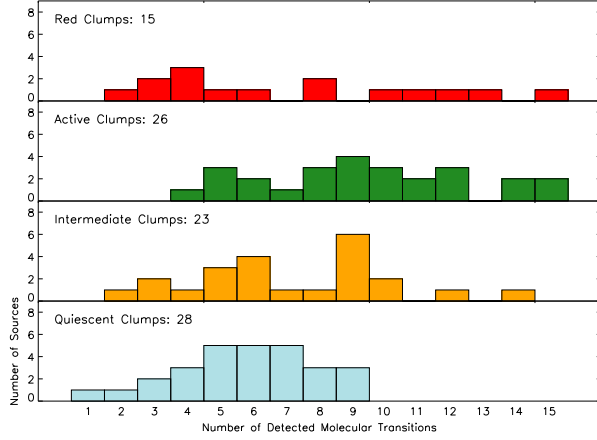


Figure 6. Histograms with the number of detected molecular transitions per source for each evolutionary stage. The name of the corresponding evolutionary stage and the number of sources contained in each histogram are given on the top left side of each panel. We find, as expected, that more evolved clumps show a rich spectrum with numerous transition lines, except that the most evolved/red clumps show a population with few detections.

a probability of 67% that active and quiescent, and 6% that red and quiescent distributions originate from the same parent populations. Although the K–S test shows that there is little difference between the active and quiescent clumps, it seems that there is an increase in ΔV from clumps with no apparent star formation to active and red clumps. We think this trend is less clearly shown by the K–S test for active and quiescent distributions because of the small number of members of each group; in spite of this, the K–S test shows a difference between the red and quiescent populations because the shape of the number distributions are more dissimilar. We conclude that the slightly broader widths found in the N_2H^+ line toward red and active clumps, compared with quiescent and intermediate clumps, is produced by the rise in the turbulence from the ongoing star formation activity.

The number distributions of HCO^+ and HNC ΔV show no clear trend, and their histograms are not presented. The range of line widths varies between 2.0 and 13.0 $km\ s^{-1}$ for HCO^+ , and between 1.0 and 7.6 $km\ s^{-1}$ for HNC . The ΔV median values of HCO^+ for quiescent, intermediate, active, and red clumps are 3.8, 4.4, 3.6, and 4.0 $km\ s^{-1}$; and for HNC are 3.2, 3.8, 3.4, and 2.8 $km\ s^{-1}$, respectively. We identify three reasons that may explain why HCO^+ and HNC do not present a similar trend to that one shown by N_2H^+ . First, the HCO^+ and HNC lines are optically thick (see Section 4.1.1) and consequently, the line widths can be broadened by opacity (e.g., Beltrán et al. 2005). Second, the HCO^+ line can show broadening and wing emission produced by molecular outflow activity. Certainly, this is what is happening in G018.82 MM3, which has a ΔV of 13.0 $km\ s^{-1}$ in the HCO^+ line. Finally, because the Mopra beam is $\sim 38''$ (0.8 pc at the average distance of 4.3 kpc), we are observing the bulk motions of the gas and some level of clumping may also be present. This also could explain why the

trend of broader N_2H^+ lines toward more evolved objects is not as clear as we expect. However, since N_2H^+ is thought to be a higher density tracer (e.g., Caselli et al.

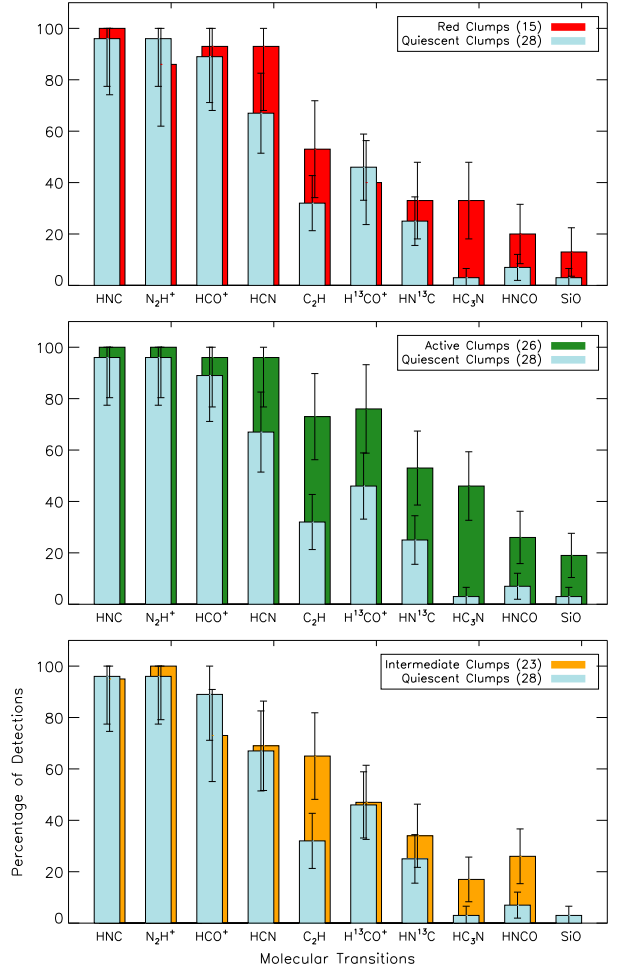


Figure 7. Detection rates of the observed molecular lines toward red, active, and intermediate clumps compared to detections rates percentages in quiescent clumps. The N_2H^+ and C_2H detection rates correspond to the $JF_1F = 123 - 012$ and $NJF = 1\frac{3}{2}2 \rightarrow 0\frac{1}{2}1$ transitions, respectively. The evolutionary sequence name and the total number of sources are given on the top right corner of each panel. HNC and N_2H^+ lines are detected in almost every IRDC clumps at every evolutionary stage. On the other hand, HC_3N , HNC , and SiO lines are predominantly detected in later stages of evolution. Error bars are the Poisson noise (i.e., the root square of the number of detections).

2002; Pirogov et al. 2003), its emission should emanate mostly from the center of the clumps and thus we still can see a weak trend.

Table 4
 Detection Rates

Molecule	Transition	Quiescent Clumps	Intermediate Clumps	Active Clumps	Red Clumps	All Clumps
HNC	$J = 1 - 0$	27 ± 5 (96%)	22 ± 5 (96%)	26 ± 5 (100%)	15 ± 4 (100%)	90 ± 10 (98%)
N ₂ H ⁺	$J = 1 - 0, F_1 = 1 - 1, F = 2 - 2$	22 ± 5 (79%)	22 ± 5 (96%)	25 ± 5 (96%)	9 ± 3 (60%)	78 ± 9 (85%)
	$J = 1 - 0, F_1 = 2 - 1, F = 3 - 2$	27 ± 5 (96%)	23 ± 5 (100%)	26 ± 5 (100%)	13 ± 4 (87%)	89 ± 9 (97%)
	$J = 1 - 0, F_1 = 0 - 1, F = 1 - 2$	8 ± 3 (29%)	12 ± 4 (52%)	17 ± 4 (65%)	5 ± 2 (33%)	42 ± 7 (46%)
HCO ⁺	$J = 1 - 0$	25 ± 5 (89%)	17 ± 4 (74%)	25 ± 5 (96%)	14 ± 4 (93%)	81 ± 9 (88%)
HCN	$J = 1 - 0$	19 ± 4 (68%)	16 ± 4 (70%)	25 ± 5 (96%)	14 ± 4 (93%)	74 ± 9 (80%)
C ₂ H	$N = 1 - 0, J = 3/2 - 1/2, F = 2 - 1$	9 ± 3 (32%)	15 ± 4 (65%)	19 ± 4 (73%)	8 ± 3 (53%)	51 ± 7 (55%)
	$N = 1 - 0, J = 3/2 - 1/2, F = 1 - 0$	1 ± 1 (4%)	3 ± 2 (13%)	10 ± 3 (39%)	4 ± 2 (27%)	18 ± 4 (20%)
	$N = 1 - 0, J = 1/2 - 1/2, F = 1 - 1$	1 ± 1 (4%)	6 ± 3 (26%)	9 ± 3 (35%)	3 ± 2 (20%)	19 ± 4 (21%)
	$N = 1 - 0, J = 1/2 - 1/2, F = 0 - 1$	1 ± 1 (4%)	1 ± 1 (4%)	4 ± 2 (15%)	2 ± 1 (13%)	8 ± 3 (9%)
H ¹³ CO ⁺	$J = 1 - 0$	13 ± 4 (46%)	11 ± 3 (48%)	20 ± 5 (77%)	6 ± 3 (40%)	50 ± 7 (54%)
HN ¹³ C	$J = 1 - 0$	7 ± 3 (25%)	8 ± 3 (35%)	14 ± 4 (54%)	5 ± 2 (33%)	34 ± 6 (37%)
HC ₃ N	$J = 10 - 9$	1 ± 1 (4%)	4 ± 2 (17%)	12 ± 4 (46%)	5 ± 2 (33%)	22 ± 5 (24%)
HNCN	$J_{K_a, K_b} = 4_{0,4} - 3_{0,3}$	2 ± 1 (7%)	6 ± 3 (26%)	7 ± 3 (27%)	3 ± 2 (20%)	18 ± 4 (20%)
SiO	$J = 2 - 1$	1 ± 1 (4%)	0 ± 0 (0%)	5 ± 2 (19%)	2 ± 1 (13%)	8 ± 3 (9%)
H ¹³ CN	$J = 1 - 0$	0 ± 0 (0%)	1 ± 1 (4%)	3 ± 2 (12%)	2 ± 1 (13%)	6 ± 2 (7%)
NH ₂ D	$J_{K_a, K_c} = 1_{1,1} - 1_{0,1}$	0 ± 0 (0%)	0 ± 0 (0%)	3 ± 2 (12%)	0 ± 0 (0%)	3 ± 2 (3%)
SO	$N_J = 2_2 - 1_1$	0 ± 0 (0%)	0 ± 0 (0%)	0 ± 0 (0%)	1 ± 1 (7%)	1 ± 1 (1%)
¹³ CS	$J = 2 - 1$	0 ± 0 (0%)	0 ± 0 (0%)	2 ± 1 (8%)	0 ± 0 (0%)	2 ± 1 (2%)
CH ₃ CN	$J = 5 - 4$	0 ± 0 (0%)	0 ± 0 (0%)	1 ± 1 (4%)	0 ± 0 (0%)	1 ± 1 (1%)

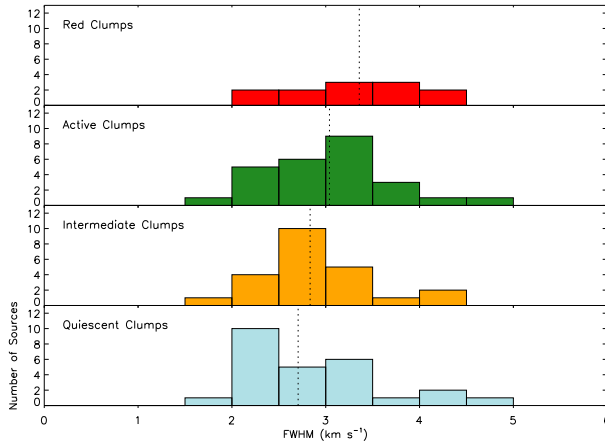


Figure 8. Histograms of the number distributions of N₂H⁺ linewidths (ΔV) for each evolutionary sequence. The name of the evolutionary stage is given on the top left corner of each panel. The vertical dashed lines indicate the median values of the ΔV for each distribution. Although the K-S test shows that active and quiescent clumps probably originate from indistinguishable parent populations, the K-S test shows that red and quiescent distributions are different. The median values of the ΔV increase with the evolution of the clumps.

Variations in N₂H⁺ line widths for different evolutionary stages toward IRDC clumps have also been observed previously by Sakai et al. (2008) and recently by Vasyunina et al. (2011). Sakai et al. (2008) observed 22 *MSX* dark objects and 7 *MSX* sources located at distances less than 4.5 kpc. *MSX* dark objects are defined by Sakai et al. (2008) as objects with 8 μ m extinction features, although some of them have *Spitzer* 24 μ m pointlike sources; thus, *MSX* dark objects correspond to our intermediate and quiescent clumps. The *MSX* sources correspond to our red clumps. Sakai et al. (2008) found that the ΔV of N₂H⁺ lines range between 0.6 and

4.0 km s⁻¹, and the mean values for *MSX* dark objects and *MSX* sources are 2.3 and 2.5 km s⁻¹, respectively. Vasyunina et al. (2011) observed 13 “quiescent” clumps (as defined by us), 11 “middle” clumps (which correspond to our intermediate and active clumps), and 13 “active” clumps (which correspond to our red clumps). They found that the range of ΔV of N₂H⁺ lines varies between 0.6 and 2.8 km s⁻¹; and “quiescent,” “middle,” and “active” clumps have ΔV mean values of 1.4, 1.7, and 2.2 km s⁻¹, respectively. If the assumption that turbulence increases with star formation activity producing broader molecular line widths in more evolved stages is correct, then the results on N₂H⁺ line widths found by Sakai et al. (2008), Vasyunina et al. (2011), and this work support the evolutionary sequence proposed by Chambers et al. (2009) for IRDC clumps.

Figure 9 shows the ΔV of the most frequently detected molecular lines against the widths of N₂H⁺. The linewidths for HNC, HCO⁺, and SiO lines show a high degree of scatter. In the case of HNC and HCO⁺, this scatter is likely produced by the high line opacities (see Section 4.1.1) and because these lines may also be tracing more external layers of the clumps. In the case of SiO, and also HCO⁺, the scatter is probably produced by molecular outflow activity, which increases the ΔV of the lines and adds extended wing emission. C₂H appears to present the best correlation with N₂H⁺. H¹³CO⁺, HN¹³C, and HC₃N have slightly narrower line widths than N₂H⁺, indicating that they trace similar optically thin gas emanating from the center of the clumps.

From Figure 9, it can be seen that there are four sources with very large linewidths in the HCO⁺ (>8.0 km s⁻¹) and SiO (>6.0 km s⁻¹) lines. They are G018.82 MM3, G018.82 MM4, G035.59 MM1, and G033.69 MM2 for HCO⁺ and G018.82 MM3, G019.27 MM2, G022.35 MM1, and G028.04 MM1 for SiO. Notably, the four sources that have large SiO linewidths are active clumps. Sakai et al. (2010) mention that larger SiO linewidths and abundances are expected in younger sources than

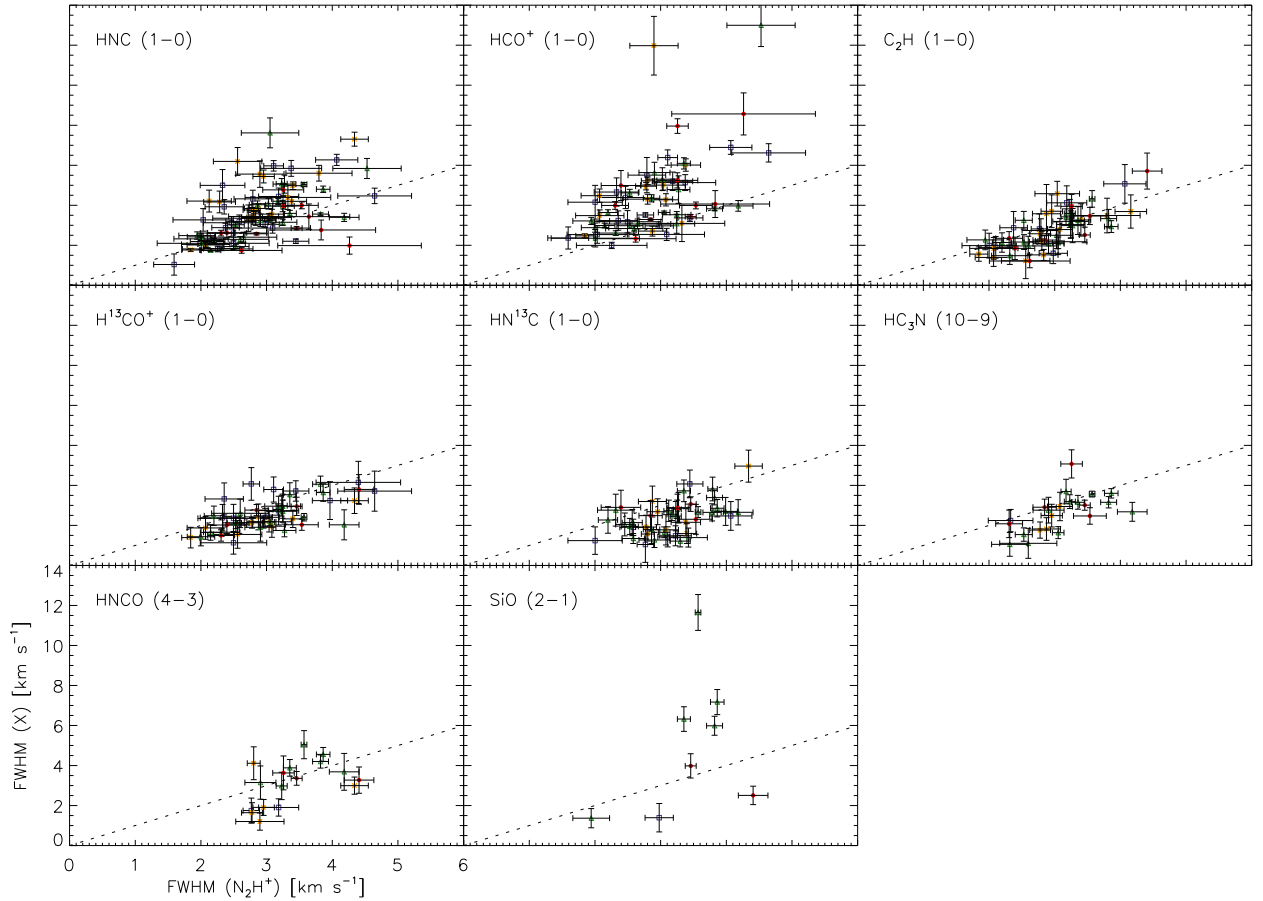


Figure 9. Correlation plots of the N_2H^+ velocity widths against the velocity widths of several molecular lines. The name of the molecular lines are given on the top left corner of each panel. The dashed line indicates unity. Blue squares correspond quiescent clumps, yellow asterisks to intermediate clumps, green triangles to active clumps, and red circles to red clumps. Linewidths of HNC, HCO^+ and SiO show a high degree of scatter. C_2H has the best correlation with N_2H^+ . H^{13}CO^+ , HN^{13}C and HC_3N have slightly narrower line widths than N_2H^+ .

MSX sources (our red clumps). However, as they also mention, strong shocks are necessary to produce SiO in the gas phase; therefore, some star formation activity is needed and the sources should be older than quiescent clumps.

3.4. Kinematic Distances

Because the N_2H^+ $JF_1F = 123 \rightarrow 012$ line has a detection rate of 97% and shows no self-absorbed profiles, we used the N_2H^+ systemic velocities of the 155 detected clumps from the initial sample to estimate kinematic distances. The distances were obtained using the Clemens (1985) rotation curve of the Milky Way, scaled to $(R_0, V_0) = (8.5 \text{ kpc}, 220 \text{ km s}^{-1})$ and included a small velocity correction (7 km s^{-1}) accounting for the measured solar peculiar motion. The distances of all clumps are listed in Table 2. To resolve the ambiguity between the near and far kinematic distances, we used the fact that IRDCs are seen as dark extinction features against the bright mid-infrared background emission. Hence, the ambiguity is resolved by assuming that all IRDCs are located at the near kinematic distance

(e.g., Simon et al. 2006b; Jackson et al. 2008). The distances to the IRDC clumps in this work were previously established by Simon et al. (2006b). They carried out a morphological matching of the MSX mid-infrared extinction with the ^{13}CO $J = 1 \rightarrow 0$ molecular line emission from the Boston University-Five College Radio Astronomy Observatory (BU-FCRAO) Galactic Ring Survey (GRS; Jackson et al. 2006). However, because the ^{13}CO $J = 1 \rightarrow 0$ emission is a low density tracer ($n_{\text{crit}} = 2 \times 10^3 \text{ cm}^{-3}$), there are typically several velocity components along one line of sight. Of the initial 155 detected IRDC clumps, the kinematic distance indicated by the high density tracer N_2H^+ ($n_{\text{crit}} = 3 \times 10^5 \text{ cm}^{-3}$) of 35 (23%) clumps differs from the distance inferred from ^{13}CO by Simon et al. (2006b). Of these sources, 17 show strong signatures of star formation and are classified as red and active clumps. Because they are isolated clumps located apart from the IRDC and at a different distance, they are not physically associated with the IRDC and were excluded from further analysis in this paper.

4. DISCUSSION

4.1. Derivation of Physical Parameters

Assuming local thermodynamic equilibrium (LTE) conditions, the total column density, N , can be derived from (e.g., Garden et al. 1991)

$$N = \frac{8\pi\nu^3}{c^3 R} \frac{Q_{\text{rot}}}{g_u A_{\text{ul}}} \frac{\exp(E_l/kT_{\text{ex}})}{[1 - \exp(-h\nu/kT_{\text{ex}})]} \int \tau_\nu dv, \quad (1)$$

where τ_ν is the optical depth of the line, g_u is the statistical weight of the upper level, A_{ul} is the Einstein coefficient for spontaneous emission, E_l is the energy of the lower state, Q_{rot} is the partition function, ν is the transition frequency, and R is the relative intensity of the brightest hyperfine transition with respect to the others. R is only relevant for hyperfine transitions because it takes into account the satellite lines correcting by their relative opacities. It is 5/9 for N_2H^+ and 5/12 for C_2H . It is equal to 1.0 for transitions without hyperfine structure.

A particular case of equation 1 is the total column density of a linear, rigid rotor molecule, which is given by (e.g., Garden et al. 1991)

$$N = \frac{3k}{8\pi^3 B\mu^2 R} \frac{(T_{\text{ex}} + hB/3k)}{(J+1)} \frac{\exp(E_J/kT_{\text{ex}})}{[1 - \exp(-h\nu/kT_{\text{ex}})]} \int \tau_\nu dv, \quad (2)$$

where μ is the permanent dipole moment of the molecule, J is the rotational quantum number of the lower state, $E_J = hBJ(J+1)$ is the energy in the level J , and B is the rotational constant of the molecule.

To calculate column densities it is necessary to estimate the optical depths of the lines. We calculate the optical depths of N_2H^+ and C_2H using their hyperfine structure, and the optical depths of HCO^+ and HNC using their isotopologues, H^{13}CO^+ and HN^{13}C . Under the assumption of LTE, all levels are populated according to the same excitation temperature (T_{ex}). We assume that T_{ex} is equal to the dust temperature (T_{D}) obtained by Rathborne et al. (2010). They determined T_{D} for 59 sources and gave lower and upper limits for 23 other sources in our sample of 92 IRDC clumps by fitting a graybody function to the spectral energy distribution (SED). For the sources with lower and upper limits, the average value of the limits was used as T_{D} . For the remaining 10 sources, without SEDs, we use the median values found by Rathborne et al. (2010) for each evolutionary sequence: 23.7, 30.4, 34.5, and 40.4 K for quiescent, intermediate, active, and red clumps, respectively. When the weakest line needed to compute the optical depth was not detected above the 3σ level (N_2H^+ $JF_1F = 112 \rightarrow 012$, C_2H $NJF = 1\frac{3}{2}1 \rightarrow 0\frac{1}{2}0$, H^{13}CO^+ , or HN^{13}C), the intensity of the line was assumed to be $3T_{\text{rms}}$. This gives an upper limit of the line intensity and thus an upper limit in the optical depth.

Actual optical depths were determined as follows. The main beam brightness temperature (T_{mb}) is the antenna temperature (T_{A}) corrected by the main beam efficiency (η_{mb}), $T_{\text{mb}} = T_{\text{A}}/\eta_{\text{mb}}$. The main beam brightness temperature of a line is related to the excitation temperature and the optical depth by

$$T_{\text{mb}} = f[J(T_{\text{ex}}) - J(T_{\text{bg}})](1 - e^{-\tau_\nu}), \quad (3)$$

where f is the filling factor, τ_ν is the optical depth of

the line, T_{bg} is the background temperature, and $J(T)$ is defined by

$$J(T) = \frac{h\nu}{k} \frac{1}{e^{h\nu/kT} - 1}. \quad (4)$$

Taking the ratio of Equation 3 evaluated for two hyperfine components or two isotopologues and assuming that the filling factors are the same, we obtain

$$\frac{1 - e^{-\tau_1}}{1 - e^{-\tau_2}} = \frac{T_{\text{mb1}}}{T_{\text{mb2}}} \left[\frac{J_2(T_{\text{ex}}) - J_2(T_{\text{bg}})}{J_1(T_{\text{ex}}) - J_1(T_{\text{bg}})} \right], \quad (5)$$

where the subscripts “1” and “2” refer to two different hyperfine components or isotopologue molecules. Defining “ r ” as the ratio between the optical depths, $r = \tau_2/\tau_1$, and utilizing the fact that the term between brackets is ~ 1 , Equation 5 becomes

$$\frac{1 - e^{-\tau_2/r}}{1 - e^{-\tau_2}} = \frac{T_{\text{mb1}}}{T_{\text{mb2}}}. \quad (6)$$

Solving this Equation numerically, we obtain the optical depth for one of the components, and by using the relationship between opacities we can obtain the optical depths of the second component.

4.1.1. Optical Depths

 N_2H^+

The opacities of the N_2H^+ hyperfine components are obtained from the ratio between the observed main beam brightness temperatures of the two brightest transitions: $JF_1F = 123 \rightarrow 012$ and $JF_1F = 112 \rightarrow 012$. Rewriting Equation 6, we obtain

$$\frac{1 - e^{-\frac{3}{5}\tau_{123-012}}}{1 - e^{-\tau_{123-012}}} = \frac{T_{\text{mb112-012}}}{T_{\text{mb123-012}}}, \quad (7)$$

where the subscripts “123 – 012” and “112 – 012” refer to the N_2H^+ hyperfine components $JF_1F = 123 \rightarrow 012$ and $JF_1F = 112 \rightarrow 012$, respectively. We have also used the opacity ratio between these two hyperfine lines, $r = \frac{\tau_{123-012}}{\tau_{112-012}} = \frac{5}{3}$, which depends only on the transition moments.

The N_2H^+ opacities were calculated for 63 IRDC clumps and the values for the main component are listed in Table 5. The main component of N_2H^+ has opacities less than 1.0 in roughly 60% of the sample. The other 40% of the sample is moderately optically thick, with a maximum opacity of 4.6. The median values for quiescent, intermediate, active, and red clumps are 0.8, 0.8, 0.5, and 1.8, respectively.

 C_2H

The optical depths of the C_2H hyperfine components are obtained using the intensity ratio between the $NJF = 1\frac{3}{2}2 \rightarrow 0\frac{1}{2}1$ and $NJF = 1\frac{3}{2}1 \rightarrow 0\frac{1}{2}0$ transitions. The opacity ratio between these two lines is $r = \frac{\tau_{12-01}}{\tau_{11-00}} = 2$ (Tucker et al. 1974). Thus, the opacity of the brightest component is given by

$$\frac{1 - e^{-\frac{1}{2}\tau_{12-01}}}{1 - e^{-\tau_{12-01}}} = \frac{T_{\text{mb11-00}}}{T_{\text{mb12-01}}}, \quad (8)$$

where the subscripts “12–01” and “11–00” refer to the C_2H hyperfine components $NJF = 1\frac{3}{2}2 \rightarrow 0\frac{1}{2}1$ and $NJF = 1\frac{3}{2}1 \rightarrow 0\frac{1}{2}0$, respectively.

The C_2H opacities were calculated for 43 IRDC clumps and the values for the brightest transition are listed in Table 5. The emission of the brightest C_2H hyperfine component is mostly moderately optically thick, with 86% of the optical depths ranging from 1.0 to 6.0. The median values of the optical depths for quiescent, intermediate, active, and red clumps are 2.9, 2.4, 2.2, and 1.4, respectively.

HCO^+ and $H^{13}CO^+$

Rewriting Equation 6, we obtain

$$\frac{1 - e^{-\tau_{12}/r}}{1 - e^{-\tau_{12}}} = \frac{T_{mb}(H^{13}CO^+)}{T_{mb}(HCO^+)}, \quad (9)$$

where “ r ” is the ratio between the optical depths, $r = \tau_{12}/\tau_{13}$, and the subscripts “12” and “13” refer to the HCO^+ and $H^{13}CO^+$ isotopologues, respectively. A way to determine “ r ” is to take the ratio of the expression for the column density (see Equation 2) evaluated for both isotopologues

$$\frac{\tau_{12}}{\tau_{13}} = \left[\frac{HCO^+}{H^{13}CO^+} \right] \frac{(kT_{ex}/hB_{13} + 1/3) \exp(E_{J_{13}}/kT_{ex})}{(kT_{ex}/hB_{12} + 1/3) \exp(E_{J_{12}}/kT_{ex})} \times \frac{[1 - \exp(-h\nu_{12}/kT_{ex})]}{[1 - \exp(-h\nu_{13}/kT_{ex})]}, \quad (10)$$

where $[HCO^+/H^{13}CO^+]$ is the isotopic abundance ratio. The isotopic abundance ratio of $[^{12}C/^{13}C]$ ranges from ~ 20 to ~ 70 (e.g., Savage et al. 2002). Assuming a constant $[HCO^+/H^{13}CO^+]$ abundance ratio of 50 for all sources, we compute the optical depths of 62 IRDC clumps. The values for HCO^+ are summarized in Ta-

ble 5. All sources have optically thick HCO^+ emission, with opacities ranging between 7 and 75. On the other hand, $H^{13}CO^+$ is optically thin in most of the sources (90%). The median values of HCO^+ optical depths for quiescent, intermediate, active, and red clumps are 30, 20, 16, and 19, respectively; and the values for $H^{13}CO^+$ are 0.6, 0.4, 0.3, and 0.4, respectively.

HNC and $HN^{13}C$

Rewriting Equation 6 and following the same procedure used for HCO^+ , we obtain

$$\frac{1 - e^{-\tau_{12}/r}}{1 - e^{-\tau_{12}}} = \frac{T_{mb}(HN^{13}C)}{T_{mb}(HNC)}, \quad (11)$$

where r is the ratio between the optical depths, $r = \tau_{12}/\tau_{13}$, and is given by

$$\frac{\tau_{12}}{\tau_{13}} = \left[\frac{HNC}{HN^{13}C} \right] \frac{(kT_{ex}/hB_{13} + 1/3) \exp(E_{J_{13}}/kT_{ex})}{(kT_{ex}/hB_{12} + 1/3) \exp(E_{J_{12}}/kT_{ex})} \times \frac{[1 - \exp(-h\nu_{12}/kT_{ex})]}{[1 - \exp(-h\nu_{13}/kT_{ex})]}, \quad (12)$$

where the subscripts “12” and “13” refer to the HNC and $HN^{13}C$ isotopologues, respectively, and $[HNC/HN^{13}C]$ is the isotopic abundance ratio.

Assuming an $[HNC/HN^{13}C]$ abundance ratio of 50, we compute the optical depths of 85 IRDC clumps. The values for HNC are summarized in Table 5. All sources have optically thick HNC emission, whereas $HN^{13}C$ is optically thin in most of the sources (95%). The median values of HNC optical depths for quiescent, intermediate, active, and red clumps are 24, 22, 18, and 16, respectively; and for $HN^{13}C$ are 0.5, 0.4, 0.3, and 0.3, respectively.

Table 5
Optical Depths and Column Densities.

IRDC Clump	Optical Depth				Column Density (cm^{-2})						
	$\tau_{N_2H^+}$	τ_{HCO^+}	τ_{HNC}	τ_{C_2H}	N_2H^+ $\times 10^{13}$	HCO^+ $\times 10^{14}$	HNC $\times 10^{14}$	C_2H $\times 10^{14}$	HC_3N $\times 10^{13}$	$HNCO$ $\times 10^{13}$	SiO $\times 10^{12}$
G015.05 MM1	1.00	29.9	26.9	2.8	1.56(0.12)	2.05(0.72)	2.27(1.09)	2.75(3.02)	...	1.67(0.69)	...
G015.05 MM2	0.04	...	59.4	...	0.71(0.15)	0.58(0.21)	2.66(1.91)
G015.05 MM3	0.60	...	28.6	...	0.36(0.10)	...	1.04(0.51)
G015.05 MM4	16.1	4.5	1.04(0.12)	0.58(0.20)	1.56(0.65)	3.06(3.29)
G015.05 MM5	0.36	35.0	52.2	...	0.52(0.16)	1.01(0.56)	2.40(1.55)
G015.31 MM2	2.89	...	69.0	...	1.18(1.25)	...	2.19(1.79)
G015.31 MM3	...	50.2	30.3	...	0.31(0.08)	0.85(0.61)	0.51(0.51)
G015.31 MM5	...	38.2	53.0	1.10(0.63)	1.36(0.95)
G018.82 MM2	2.16	44.6	43.5	...	2.24(2.25)	3.20(1.94)	3.45(2.10)
G018.82 MM3	2.27	37.7	27.9	...	6.07(6.15)	10.10(5.24)	6.71(3.14)
G018.82 MM4	0.12	75.0	45.3	...	1.06(0.18)	8.50(6.72)	5.02(2.85)	0.98(1.04)	...
G018.82 MM6	0.12	1.22(0.12)	0.52(0.19)	0.80(0.35)
G019.27 MM2	0.81	...	33.8	5.6	2.18(0.15)	...	4.09(1.40)	4.15(4.59)
G022.35 MM1	0.31	14.4	20.9	...	0.40(0.10)	0.85(0.33)	1.13(0.47)
G022.35 MM2	33.2	2.02(1.07)
G023.60 MM7	1.64	...	27.6	...	4.13(4.07)	...	3.50(1.67)
G023.60 MM9	0.56	...	29.3	2.4	0.68(0.11)	...	1.47(0.71)	1.51(2.16)
G024.08 MM2	0.99	43.0	26.4	...	0.70(0.12)	1.77(0.71)	2.51(1.12)
G024.08 MM3	1.27	31.5	24.1	...	0.93(0.92)	1.78(0.89)	1.91(0.85)
G024.08 MM4	0.27	66.5	31.1	...	0.48(0.13)	2.43(2.20)	1.84(0.94)
G024.33 MM2	25.5	...	3.06(0.18)	1.37(0.36)	6.16(1.17)	4.27(1.10)	...
G024.33 MM3	1.9	2.65(0.17)	1.38(0.35)	0.85(0.29)	3.41(4.60)	...	2.81(0.90)	3.96(1.41)
G024.33 MM4	1.57(0.13)	0.79(0.30)	0.78(0.28)
G024.33 MM5	0.26	3.2	2.17(0.15)	2.81(0.46)	0.79(0.29)	2.63(3.99)	...	5.44(0.94)	...

Table 5 — *Continued*

IRDC Clump	Optical Depth				Column Density (cm^{-2})						
	$\tau_{\text{N}_2\text{H}^+}$	τ_{HCO^+}	τ_{HNC}	$\tau_{\text{C}_2\text{H}}$	N_2H^+ $\times 10^{13}$	HCO^+ $\times 10^{14}$	HNC $\times 10^{14}$	C_2H $\times 10^{14}$	HC_3N $\times 10^{13}$	HNCO $\times 10^{13}$	SiO $\times 10^{12}$
G024.33 MM7	0.67	15.0	10.3	1.2	0.93(0.09)	1.22(0.23)	1.06(0.39)	0.61(1.20)	1.36(0.74)
G024.33 MM8	...	13.2	15.8	1.40(0.53)	2.62(1.01)
G024.33 MM9	...	10.9	11.5	2.30(0.89)	3.48(1.36)
G024.33 MM11	0.59	29.9	23.9	...	1.51(0.10)	2.82(0.62)
G024.60 MM2	0.92	22.4	16.4	1.1	1.24(0.10)	1.51(0.49)	1.48(0.63)	1.16(0.40)	0.35(0.12)
G025.04 MM2	...	13.2	18.3	...	0.63(0.11)	1.26(0.51)	1.70(0.73)
G025.04 MM4	0.06	8.7	24.6	1.0	2.44(0.11)	1.51(0.54)	4.30(1.01)	1.09(2.22)	...	3.12(0.66)	...
G027.75 MM2	3.17	1.01(1.02)
G027.94 MM1	1.39	...	22.9	3.1	1.66(1.66)	...	1.97(0.68)	1.94(3.13)
G028.04 MM1	1.15	24.1	60.7	1.3	2.27(2.23)	2.24(0.96)	5.50(2.66)	1.27(2.27)	0.38(0.12)	2.88(0.84)	...
G028.08 MM1	1.25	...	40.7	...	0.63(0.63)	...	1.92(1.02)
G028.23 MM1	3.62	3.12(3.14)	1.00(0.34)	0.77(0.27)
G028.28 MM4	0.88	13.9	11.1	3.0	1.53(0.13)	1.83(0.38)	1.65(0.60)	2.68(3.09)
G028.37 MM1	20.6	1.9	4.60(0.15)	2.51(0.39)	5.72(0.97)	4.31(2.38)	1.45(0.14)	9.93(0.88)	16.00(1.36)
G028.37 MM2	0.46	...	24.6	3.0	2.51(0.18)	2.42(0.45)	6.37(1.76)	4.54(6.44)	0.49(0.21)	3.61(1.50)	...
G028.37 MM4	0.06	12.8	11.8	4.8	4.69(0.19)	2.90(0.30)	4.37(0.47)	6.30(5.60)	0.85(0.11)	8.05(0.63)	13.90(0.98)
G028.37 MM6	0.19	22.2	20.3	2.3	2.67(0.10)	2.72(0.52)	2.88(0.46)	1.80(1.89)	0.77(0.12)	4.30(0.51)	10.20(0.90)
G028.37 MM9	...	21.9	15.0	...	1.52(0.11)	1.99(0.34)	1.52(0.29)
G028.37 MM11	0.23	...	41.8	3.3	1.05(0.20)	0.82(0.28)	7.21(3.80)	2.63(4.22)
G028.37 MM12	1.37	65.8	74.0	...	0.89(0.90)	2.42(1.38)	3.61(2.86)	...	0.31(0.15)
G028.37 MM13	3.32	1.46(1.58)
G028.53 MM3	1.73	19.4	23.7	...	2.47(2.42)	2.13(0.64)	2.38(1.04)
G028.53 MM5	4.45	46.0	46.7	...	2.90(3.03)	1.50(1.02)	3.43(2.01)
G028.53 MM7	49.0	...	1.10(0.12)	0.91(0.26)	3.47(1.21)
G028.53 MM8	...	69.4	37.1	1.5	1.00(0.14)	3.54(2.78)	3.44(1.77)	2.02(1.15)
G028.53 MM9	0.81	13.9	15.0	...	1.88(0.16)	2.38(0.95)	3.08(1.01)
G028.53 MM10	0.10	13.7	17.2	2.9	2.04(0.20)	2.83(1.08)	4.90(1.46)	5.05(6.87)
G028.67 MM1	...	31.0	31.2	1.64(0.82)	2.95(1.41)
G028.67 MM2	0.83	...	47.7	...	0.71(0.10)	...	2.64(1.57)
G030.14 MM1	4.58	37.8	32.6	...	1.36(1.50)	1.18(0.68)	1.61(0.83)
G030.57 MM1	0.11	...	19.6	1.1	4.42(0.15)	...	3.85(1.22)	2.64(4.13)	0.85(0.15)	2.86(0.98)	...
G030.57 MM3	0.42	...	45.2	6.0	0.98(0.18)	...	6.33(3.59)	2.39(3.67)
G030.97 MM1	...	16.4	9.4	...	3.64(0.14)	5.17(0.50)	4.04(0.67)	...	0.37(0.12)
G031.97 MM5	0.04	...	15.2	3.5	2.33(0.13)	1.25(0.29)	3.53(1.15)	2.93(3.80)
G031.97 MM7	0.45	7.3	14.5	3.5	1.69(0.10)	1.20(0.23)	3.00(2.81)	2.14(3.40)	...	1.00(0.56)	...
G031.97 MM8	9.5	...	3.43(0.20)	...	3.41(1.18)
G033.69 MM1	...	9.8	11.4	...	3.56(0.11)	1.70(0.25)	2.93(0.34)	...	0.96(0.13)	4.55(0.59)	5.29(1.01)
G033.69 MM2	...	17.1	14.6	0.8	3.19(0.21)	4.53(1.84)	4.48(1.14)	3.55(0.49)	1.01(0.16)	4.31(1.21)	...
G033.69 MM3	...	18.5	16.4	...	2.40(0.28)	3.61(1.51)	5.18(2.09)
G033.69 MM4	...	12.4	16.2	...	3.05(0.21)	1.76(0.64)	3.37(0.83)	...	0.56(0.20)	3.07(1.02)	...
G033.69 MM5	...	31.6	18.3	2.9	2.15(0.24)	3.85(1.91)	4.23(1.76)	3.75(3.05)
G033.69 MM11	...	12.1	13.9	4.0	...	2.53(0.95)	3.99(1.52)	1.48(2.87)
G034.43 MM1	0.42	...	18.0	1.7	13.70(0.21)	4.77(0.48)	13.60(1.58)	7.75(4.71)	3.33(0.21)	8.59(1.43)	34.70(2.09)
G034.43 MM5	0.67	...	30.0	...	2.98(0.09)	1.92(0.25)	5.23(0.79)	...	0.54(0.12)
G034.43 MM7	...	21.6	18.9	1.9	1.11(0.11)	1.07(0.33)	2.29(0.60)	2.06(2.92)	0.21(0.12)
G034.43 MM8	...	65.7	19.0	3.9	1.53(0.17)	2.71(1.21)	2.55(1.01)	3.56(5.98)
G034.77 MM1	2.20	27.9	11.2	...	4.09(4.04)	4.52(0.79)	2.44(0.80)	...	0.47(0.13)
G034.77 MM3	0.25	...	22.4	4.1	0.88(0.15)	0.50(0.18)	2.78(1.17)	3.01(5.16)
G035.39 MM7	0.18	27.9	17.6	2.1	2.41(0.17)	6.00(0.94)	3.81(0.82)	4.38(4.13)	0.32(0.15)
G035.59 MM1	4.18	31.0	40.8	...	2.84(3.10)	4.38(2.19)	1.77(1.10)
G035.59 MM2	...	21.8	11.6	...	0.72(0.10)	1.82(0.57)	1.09(0.41)
G035.59 MM3	0.42	7.8	10.5	2.4	1.00(0.23)	1.12(0.29)	1.12(0.47)	1.82(2.20)	0.14(0.19)
G036.67 MM1	3.22	68.4	19.7	4.3	0.99(1.02)	1.58(1.34)	1.02(0.60)	1.58(1.57)
G036.67 MM2	...	20.2	18.1	0.65(0.28)	1.15(0.48)
G038.95 MM1	0.12	26.9	9.6	1.2	1.34(0.10)	4.27(0.65)	1.69(0.51)	2.41(1.94)	0.47(0.19)	0.92(0.53)	...
G038.95 MM2	0.92	19.7	11.1	...	1.72(0.20)	4.64(1.06)	2.45(0.92)	...	0.35(0.17)
G038.95 MM3	2.44	18.5	14.0	0.4	2.98(2.97)	3.40(0.87)	2.35(0.92)	2.80(0.40)
G038.95 MM4	1.66	10.4	13.8	1.0	1.97(1.99)	1.83(0.68)	2.34(0.92)	2.16(0.39)	2.48(1.80)
G053.11 MM1	0.56	10.5	4.5	...	3.11(0.25)	4.74(0.48)	1.97(0.59)	...	0.80(0.14)
G053.11 MM2	1.05	13.6	9.6	1.1	2.76(2.77)	2.80(0.56)	1.87(0.53)	1.62(0.62)
G053.11 MM4	0.52	23.0	7.1	0.2	1.11(0.17)	4.03(0.61)	1.45(0.39)	0.94(0.36)	0.16(0.12)
G053.11 MM5	4.24	11.0	12.4	0.9	2.90(2.96)	1.26(0.47)	1.54(0.58)	1.08(0.25)
G053.25 MM1	...	7.8	5.7	1.5	1.44(0.14)	1.38(0.45)	1.20(0.42)	1.54(2.06)
G053.25 MM3	1.79	15.3	10.4	4.4	1.37(1.44)	1.49(0.62)	1.35(0.52)	3.10(5.18)
G053.25 MM4	0.25	12.4	5.8	...	1.62(0.15)	2.44(0.56)	1.23(0.43)
G053.25 MM5	...	21.4	10.7	4.8	...	2.55(0.88)	1.38(0.52)	2.05(4.63)
G053.25 MM6	1.46	13.3	7.5	...	3.84(3.88)	2.64(0.62)	1.65(0.62)
G053.31 MM2	2.69	11.2	13.3	...	1.24(1.23)	0.67(0.25)	1.00(0.39)

4.1.2. Column Densities

The column densities of N_2H^+ , HCO^+ and HNC are calculated using equation 2. The SiO molecule is also a linear, rigid rotor. Thus, we can also use equation 2 to estimate SiO column densities. However, since we observed only one SiO isotopologue, we need to assume that the SiO emission is optically thin and the filling factor is 1.0 (which gives us the beam-averaged column density). Therefore, replacing equation 3 in equation 2, we obtain

$$N = \frac{3k}{8\pi^3 B \mu^2 R} \frac{(T_{\text{ex}} + hB/3k)}{(J+1)} \frac{\exp(E_J/kT_{\text{ex}})}{[1 - \exp(-h\nu/kT_{\text{ex}})]} \times \frac{1}{[J(T_{\text{ex}}) - J(T_{\text{bg}})]} \int T_{\text{mb}} dv. \quad (13)$$

The values of the parameters used in the column density calculations (permanent dipole moment, rotational constant) of N_2H^+ , HCO^+ , HNC , and SiO are summarized in Table 6.

Table 6Parameters used for N_2H^+ , HCO^+ , HNC , and SiO Column Density Calculations

Molecule	Dipole Moment μ (D)	Rotational Constant B (GHz)	References
N_2H^+	3.40	46.586871	1, 2, 3
HCO^+	3.89	44.594423	4, 5, 6
H^{13}CO^+	3.89	43.377302	4, 5, 6
HNC	3.05	45.331980	7, 8
HN^{13}C	3.05	43.545600	7, 8
SiO	3.10	21.711979	9, 10

Note. — References. (1) Botschwina (1984); (2) Havenith et al. (1990); (3) Pagani et al. (2009); (4) Botschwina et al. (1993); (5) Yamaguchi et al. (1994); (6) Lattanzi et al. (2007); (7) Blackman et al. (1976); (8) van der Tak et al. (2009); (9) Raymond et al. (1970); (10) Mollaghababa et al. (1991)

The column densities of the remaining molecules (C_2H , HC_3N , HNCO) are determined using equation 1. Although C_2H is a linear molecule, its rotational energy levels are described by the rotational quantum number N , instead of J . HC_3N is also linear and its partition function is the same used for diatomic, linear molecules (Blake et al. 1987); we have not included the factor 3 due to the nuclear spin degeneracy because the hyperfine structure is not resolved. On the other hand, HNCO is a standard asymmetric top molecule with a different partition function (Blake et al. 1987). For C_2H the column density was calculated using the optical depths obtained in Section 4.1.1. For HC_3N and HNCO , the emission was assumed to be optically thin and the filling factor was used to be equal to 1.0. The values of the parameters used in the column density calculations (partition function, rotational constants, statistical weight, Einstein coefficient for spontaneous emission, and energy of the lower state) of C_2H , HC_3N and HNCO are summarized in Table 7.

Upper limits to the column densities of the most commonly detected molecular lines (N_2H^+ , HCO^+ , HNC) were estimated when they were not detected over the 3σ level. In the case of the optically thick HCO^+ and HNC

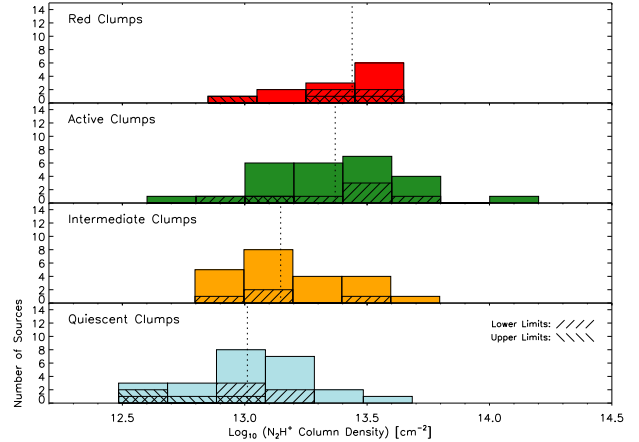


Figure 10. Histograms of the number distributions of N_2H^+ column densities for each evolutionary sequence. The name of the evolutionary stage is given on the top left corner of each panel. The vertical dashed lines indicate the median values of the column densities for each distribution. The diagonal patterns indicate the portions of the histograms that correspond to upper and lower limits (see bottom panel, right side). The median values and the K-S test suggest that column densities increase with the evolution of the clumps. Median values of the column densities are given in Table 8.

emission lines, the limits were obtained first for their isotopologues (H^{13}CO^+ and HN^{13}C). Then by using the isotopic abundance ratio we calculated the column densities for HCO^+ and HNC . In all non-detections, the emission was assumed to be optically thin, with $T_{\text{mb}} = 3T_{\text{rms}}$, and ΔV equal to 2.0 km s^{-1} .

Additionally, lower limits to the column densities were estimated for N_2H^+ and HCO^+ when our normal approach was not applicable. For N_2H^+ , the intensity ratio between the two brightest components, which is used to derive opacities, should not be higher than its value in the optically thin limit, $5/3$. However, in some cases, this ratio exceeds the optically thin limit, but nevertheless remains consistent with $5/3$ within the uncertainties. To calculate a lower limit for the column density, the main N_2H^+ component was assumed to be optically thin. For HCO^+ , in several cases the spectra show self-absorbed profiles, and no Gaussian fit was performed. Lower limits to the column densities were computed using the H^{13}CO^+ emission line and assuming that its emission is optically thin. Then, using the $[\text{HCO}^+/\text{H}^{13}\text{CO}^+]$ isotopic abundance ratio, we obtain the HCO^+ column densities.

Derived column densities using the optical depths obtained in Section 4.1.1 were multiplied by the filling factor to get the beam-averaged column density. The filling factor was calculated from Equation 3. Column densities for N_2H^+ , HCO^+ , HNC , SiO , C_2H , HC_3N , and HNCO molecules (including all limits) are listed in the Table 5. Median values of the column densities for each evolutionary sequence (excluding limits when the lines are not detected above the 3σ level) are shown in Table 8.

 N_2H^+

Figure 10 shows the number distributions of the N_2H^+ column densities for each evolutionary sequence. The K-S test gives a probability of 0.09% that quiescent and ac-

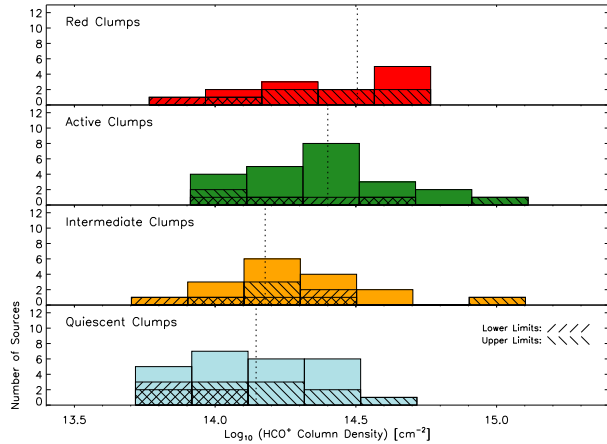


Figure 11. Histograms of the number distributions of HCO^+ column densities for each evolutionary sequence. The name of the evolutionary stage is given on the top left corner of each panel. The vertical dashed lines indicate the median values of the column densities for each distribution. The diagonal patterns indicate the portions of the histograms that correspond to upper and lower limits (see bottom panel, right side). The median values and the K-S test suggest that column densities increase with the evolution of the clumps. Median values of the column densities are given in Table 8.

tive clump distributions originate from the same parent population. Figure 10 shows a trend of increasing column densities with the evolution of the clump, which is confirmed by the median values (see Table 8) and the K-S test probability. This trend does not necessarily imply a change in the chemistry. An increase of the N_2H^+ column density could simply indicate that the total H_2 column density increases while maintaining constant chemical composition. In Sections 4.2 and 4.4 we discuss the molecular abundances, which more definitively show chemical variations. This argument applies to all the molecules discussed in this section. Sakai et al. (2008) obtained N_2H^+ column densities over a sample of 11 *Spitzer* and *MSX* dark objects (no 24 and 8 μm emission, respectively) that we can compare with our quiescent clumps. Pirogov et al. (2003) obtained N_2H^+ column densities of 34 clumps, where massive stars have already formed, that we can compare with our active clumps. Table 9 summarizes the results of previous works, which are in good agreement with our results.

HCO^+ and H^{13}CO^+

Figure 11 shows the number distributions of the HCO^+ column densities for each evolutionary stage. The K-S test gives us a probability of 2% that quiescent and active distributions originate from the same parent population. Figure 11 shows a trend of increasing column densities with the evolution of the clump, which is supported by the median values (see Table 8) and the K-S test probability. Sakai et al. (2010) and Purcell et al. (2006) obtained H^{13}CO^+ and HCO^+ column densities toward 20 and 79 massive clumps, respectively, associated with IR emission, methanol masers and UC HII regions. We compare this sample with our active and red cores in Table 9. The high HCO^+ column densities obtained by Sakai et al. (2010) and Purcell et al. (2006) confirm

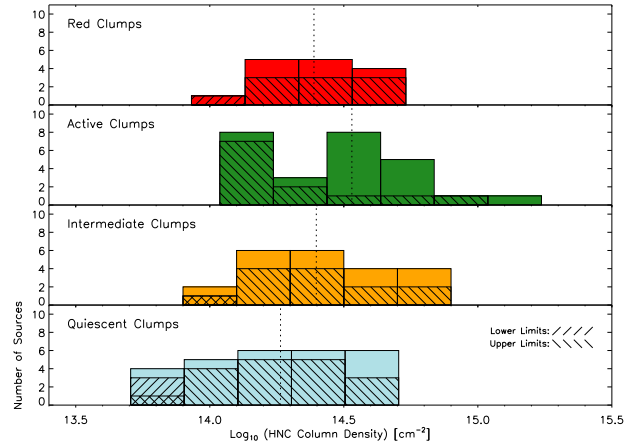


Figure 12. Histograms of the number distributions of HNC column densities for each evolutionary sequence. The name of the evolutionary stage is given on the top left corner of each panel. The vertical dashed lines indicate the median values of the column densities for each distribution. The diagonal patterns indicate the portions of the histograms that correspond to upper and lower limits (see bottom panel, right side). The median values and the K-S test suggest that column densities increase with the evolution of the clumps, from quiescent, to intermediate, to active clumps. Median values of the column densities are given in Table 8.

the trend that HCO^+ column densities increase with the evolution of the clumps, as seen in Figure 11.

HNC and HN^{13}C

Figure 12 shows the number distributions of the HNC column densities for each evolutionary stage. The K-S test gives a probability of 5% that quiescent and active distributions originate from the same parent population. Figure 12 shows a weaker trend (compared with N_2H^+ and HCO^+) of increasing column densities from quiescent to active clumps. There are only a few systematic studies of HNC toward a large sample of massive star forming or IRDC clumps. Sakai et al. (2010) observed HN^{13}C toward 20 massive clumps that we can compare with our active clumps. Their values, showed in Table 9, are in good agreement with our results.

C_2H

Figure 13 shows the number distributions of the C_2H column densities for each evolutionary sequence. The K-S test gives us a probability of 38% that active and quiescent distributions originate from the same parent population. Figure 13 shows that the trend of increasing column densities with the evolution of the clumps is less evident for C_2H than for previous molecules. Although the median values obtained for each evolutionary sequence support this trend, the K-S test probability is not low enough to be confident. Table 9 compares the column densities obtained for 20 massive clumps by Sakai et al. (2010) with our active clumps, which are in a reasonable agreement.

HC_3N

The median values for the HC_3N column densities are summarized in Table 8. HC_3N emission was detected only in one quiescent clump, G028.37 MM12, whose col-

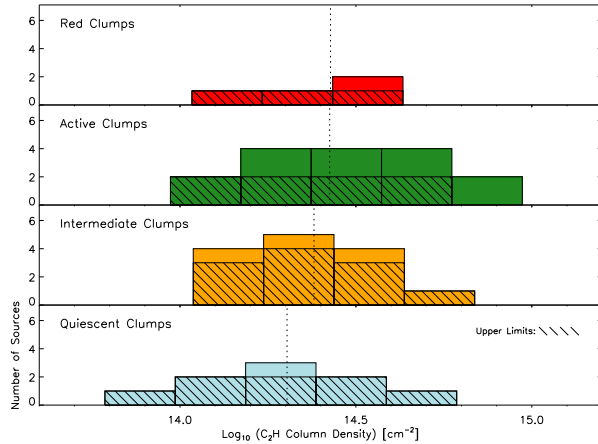


Figure 13. Histograms of the number distributions of C_2H column densities for each evolutionary sequence. The name of the evolutionary stage is given on the top left corner of each panel. The vertical dashed lines indicate the median values of the column densities for each distribution. The diagonal patterns indicate the portions of the histograms that correspond to upper limits. The median values slightly increase with the evolution of the clumps; however, the K-S test shows this variation is not statistically significant. Median values of the column densities are given in Table 8. Column density was $3.05 \times 10^{12} \text{ cm}^{-2}$. Sakai et al. (2008) obtained HC_3N column densities for 7 *Spitzer* and *MSX* dark objects (no 24 and 8 μm emission, respectively). Their values are comparable to that found in our one quiescent clump (see Table 9).

HNCO

The median values for the $HNCO$ column densities are summarized in Table 8. Zinchenko et al. (2000) calculated $HNCO$ column densities toward 20 massive star forming clumps using rotational diagrams. These sources were selected based on the presence of water masers and strong SiO emission, indicating they are currently forming stars. They obtained higher values than those found in our IRDC sample (Table 9). This may be explained by the warmer rotational temperatures (median of 88 K) obtained by Zinchenko et al. (2000).

SiO

The median values for the SiO column densities are summarized in Table 8. SiO emission was detected in no intermediate clumps and only in one quiescent clump, G024.33 MM7, whose column density is $1.36 \times 10^{12} \text{ cm}^{-2}$. Sakai et al. (2010) and Miettinen et al. (2006) obtained SiO column densities for 17 and 15 high-mass star-forming clumps, respectively, associated with IR and maser emission and UC HII regions (See Table 9). Their values agree with those we calculated for active clumps. Red clumps, however, have lower column densities.

4.2. Chemistry

In order to study the chemistry toward the IRDC clumps, and investigate if the different evolutionary sequences proposed by Chambers et al. (2009) are chemically distinguishable, we calculate molecular abundances using the 1.2 mm continuum emission obtained by Rathborne et al. (2006) and abundance ratios of selected species.

4.2.1. Molecular Abundances

To estimate molecular abundances with respect to molecular hydrogen, we take the ratio between the column density of a given molecule and the H_2 column density derived from dust emission. Observations of 1.2 mm dust continuum emission were obtained by Rathborne et al. (2006) with an angular resolution of $11''$. In order to calculate the molecular abundances, we smoothed the continuum emission data to the angular resolution of the molecular line data at 3 mm, $38''$. The resulting 1.2 mm peak flux, H_2 column densities and molecular abundances for the N_2H^+ , HCO^+ , HNC , C_2H , HC_3N , $HNCO$, and SiO lines (including limits for N_2H^+ , HCO^+ , and HNC) are listed in Table 10. In general, the number distributions of abundances show few differences between the evolutionary sequences, with the exception of N_2H^+ and HCO^+ (Figure 14 and 15). The K-S test gives a probability of 0.09% and 1.2% that quiescent and active distributions originate from the same parent populations for N_2H^+ and HCO^+ , respectively. On the other hand, the evolutionary status of the clumps is not evidently distinguishable from the abundances of HNC , C_2H , HC_3N , $HNCO$, and SiO , although their median values change with the evolution of the clumps. Median values of the molecular abundances for each evolutionary sequence (excluding the limits when the lines are not detected) are shown in Table 8.

Vasyunina et al. (2011) observed 37 IRDC clumps in the fourth quadrant with the Mopra telescope. They also obtained molecular abundances for N_2H^+ , HCO^+ , HNC , SiO , C_2H , HC_3N , and $HNCO$. Despite a couple of different assumptions (Vasyunina et al. (2011) did not smooth their 1.2 mm dust continuum emission to the angular resolution of Mopra ($38''$) and they used NH_3 temperatures), the abundances they find are in good agreement with the abundances determined in this work, except for HNC . They determined HNC abundances about an order of magnitude lower than our values. Because Vasyunina et al. (2011) did not have the isotopologue $HN^{13}C$, they assumed that the emission was optically thin in order to get an estimate of the column density. However, as we discussed in Section 4.1.1, the optically thin assumption is not valid for HNC in IRDCs because the emission is optically thick.

4.2.2. Abundance Ratios

Molecular abundance ratios that can be used to estimate the age and mark the evolutionary stages of star-forming regions are known as “chemical clocks.” Only molecules that show differential abundances with time can be used to evaluate the evolutionary status of a star-forming region. Chemical clocks have been studied in depth in low-mass star-forming regions (e.g., Emprechtinger et al. 2009); the concept of chemical clocks has been less developed in the context of high-mass star-forming regions. Recent studies in small samples of high-mass star-forming regions show that chemical clocks can be extended to their high-mass counterpart (e.g., Fontani et al. 2011). In this section, we explore the idea that N_2H^+/HCO^+ and N_2H^+/HNC ratios can be used as chemical clocks. We choose this set of lines because they reveal the clearest significant chemical variations.

Table 7
Parameters used for C₂H, HC₃N and HNCO Column Density Calculations

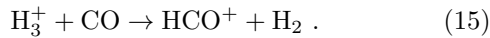
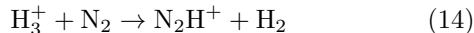
Molecule	Q_{rot}	Rot. Const. (GHz)	g_u	A_{ul} ($\times 10^{-6}$ s ⁻¹)	E_l/k
C ₂ H	$kT_{ex}/hB + 1/3$	$B = 43.674518^{(1)}$	5.0	1.52757	0.00216
HC ₃ N	$kT_{ex}/hB + 1/3$	$B = 4.5490586^{(2)}$	21.0	58.1300	19.6484
HNCO	$[\pi(kT_{ex})^3/(h^3ABC)]^{1/2}$	$A = 918.417805^{(3)}$ $B = 11.071010^{(3)}$ $C = 10.910577^{(3)}$	9.0	8.78011	6.32957

Note. — References. (1) Padovani et al. (2009); (2) Thorwirth et al. (2000); (3) Lapinov et al. (2007). Values for g_u , A_{ul} and E_l/k were obtained from The Cologne Database for Molecular Spectroscopy (CDMS) (Müller et al. 2001, 2005).

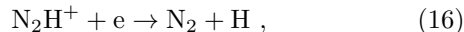
N₂H⁺ and HCO⁺

It has been suggested that the line and abundance ratios of N₂H⁺ and HCO⁺ are anticorrelated, varying spatially over a given cloud and for different sources. The change in the N₂H⁺/HCO⁺ ratio was first noted by Turner & Thaddeus (1977) and Snyder et al. (1977), and recently by Kim et al. (2006) and Lo et al. (2009); however, it has not been studied in a large sample of star-forming clumps. Although we cannot examine spatial variations, due to our single-pointing observations, we can test whether the abundance ratios show differences for the four evolutionary stages proposed by Chambers et al. (2009).

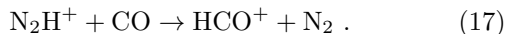
According to ion-molecule schemes of dense molecular clouds (e.g., Snyder et al. 1977; Jørgensen et al. 2004), N₂H⁺ and HCO⁺ are formed primary through reactions with H₃⁺:



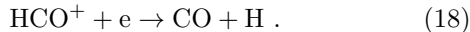
The main destruction mechanisms for N₂H⁺ are electron recombination, when CO is frozen out on dust grains,



and by reacting with CO, when CO is found in the gas-phase at standard abundances ($[\text{CO}/\text{H}_2] \sim 10^{-4}$),



The dominant removal mechanism for HCO⁺ is electron recombination



Chemical models of low-mass star-forming regions (e.g., Lee et al. 2004; Jørgensen et al. 2004) and one of a massive star-forming region (Kim et al. 2006) show that the N₂H⁺/HCO⁺ ratio is high in early stages due to HCO⁺ depletion (because most of the CO is frozen out) and is low in later stages when CO is evaporated from the dust grains ($T \sim 20$ -25 K). Because CO is both the main supplier of HCO⁺ and the main destroyer of N₂H⁺, the theory suggests that the HCO⁺ abundance increases with respect to N₂H⁺ as the clump evolves to a warmer phase. It is notable, for reasons not yet fully understood,

that N₂H⁺ is resistant to depletion in cold, dense regions. For a long time, it was thought that N₂, the main supplier of N₂H⁺, had a lower binding strength to the grain surface than CO. However, recent measurements show that they are similar (Öberg et al. 2005). Hence, the chemical network that dominates the formation and destruction of N₂H⁺ and HCO⁺ in early stages of star formation is given by Equations 14, 15, 16 and 18, but for more evolved stages, Equation 16 becomes less important and is replaced by Equation 17. A complete chemical network of H₃⁺, N₂H⁺, and HCO⁺, including formation and destruction rates, is presented in detail by Jørgensen et al. (2004).

Figure 16 shows the number distributions of the N₂H⁺/HCO⁺ abundance (or column density) ratio for each evolutionary sequence. The median values for each distribution are 0.08, 0.12, 0.10, and 0.07 for quiescent, intermediate, active, and red clumps, respectively. As can be seen from the Figure 16, quiescent clumps do not present the predicted abundance ratio to follow the trend of decreasing N₂H⁺/HCO⁺ ratio with the evolution of the clumps; their ratios are more randomized. For this reason, we use the K-S test for the intermediate and red clump distributions. The test shows that the probability of both populations being the same is low (3%). The values of the median and the K-S test probability support the theoretical idea that the N₂H⁺/HCO⁺ abundance ratio acts as a chemical clock (at least for the intermediate, active, and red clumps); however, why this trend does not extend to quiescent clumps is unclear. We note that the relative abundance between N₂H⁺ and HCO⁺ acts as a chemical clock despite the abundances of both molecules independently increasing with the evolution of the clumps. We stress that a large number of values used in the histograms are limits and that a number of assumptions have gone into calculating the column densities and abundances. A sample with a larger number of strong detections would be very helpful for confirming these trends.

The trend of decreasing N₂H⁺/HCO⁺ ratio with the evolution of the clumps may not extend to quiescent clumps due to one or a combination of the following reasons: (a) the sample of quiescent clumps could contain clumps with embedded star formation that was not detected by Spitzer, (b) CO has not had time to freeze out on dust grains, (c) the theoretical predictions at the very early stages are incorrect, and/or (d) due to the large beam of Mopra, we are probably detecting contaminating, diffuse emission which is not directly related to the star-forming process in the center of the clumps. Considering the last point, since the size of the Mo-

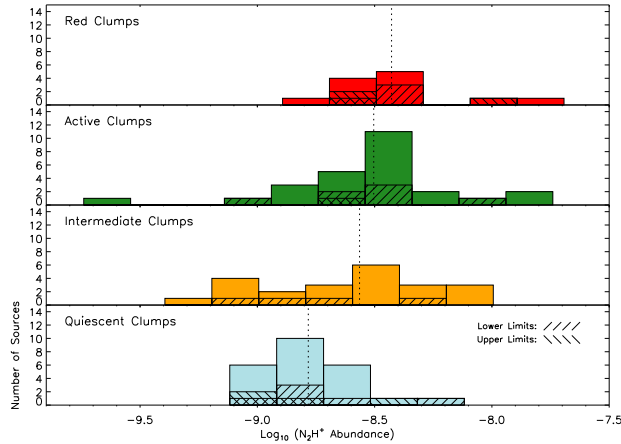


Figure 14. Histograms of the number distributions of N_2H^+ abundances for each evolutionary sequence. The name of the evolutionary stage is given on the top left corner of each panel. The vertical dashed lines indicate the median values of the abundances for each distribution. The diagonal patterns indicate the portions of the histograms that correspond to upper and lower limits (see bottom panel, right side). The median values and the K-S test suggest that abundances increase with the evolution of the clumps, as it is also found by Busquet et al. (2011) in their chemical modeling. Median values of the column densities are given in Table 8.

pra beam is $38''$, we are typically observing emission on physical scales ~ 0.8 pc. Typical sizes of clumps in high-mass star-forming regions and in IRDCs are ~ 0.4 pc (Faúndez et al. 2004) and ~ 0.5 pc (Rathborne et al. 2006), respectively. This shows that we are not only tracing the densest regions associated with star formation, but also the environment between clumps. Lee et al. (2004) predict that the variation of the molecular abundances is much larger when we consider small scales inside the clumps. Further studies at higher angular resolution, using interferometers, are needed to understand the discrepancy shown by quiescent clumps.

N_2H^+ and HNC

Figure 17 shows the $\text{N}_2\text{H}^+/\text{HNC}$ abundance ratio for each evolutionary stage. The median values for each distribution are 0.06, 0.06, 0.08, and 0.08 for quiescent, intermediate, active, and red clumps, respectively. The K-S test for the quiescent and active clump distributions shows that the probability of both populations being the same is low (5%). The median values and the K-S test suggest that there is a trend of increasing $\text{N}_2\text{H}^+/\text{HNC}$ abundance ratio with the evolution of the clumps. We note that N_2H^+ and HCO^+ are strongly linked because of their pathways of formation and destruction; on the other hand, a connection between N_2H^+ and HNC is less evident. The trend between these two molecules suggests that HNC may be preferentially formed in cold gas.

Other Abundance Ratios

It is expected that abundances of SiO and more complex molecules, such as HC_3N and HNC, increase in more evolved star-forming regions. In evolved regions, these molecules or their parent molecules are released from the dust grains by shocks and sublimation due to the temperature increase. In fact, the abundance ratio

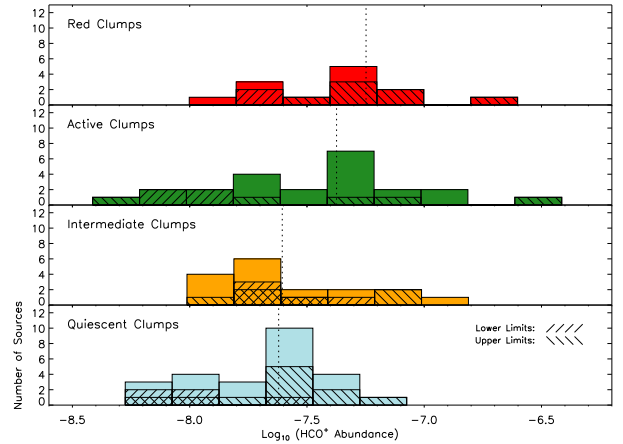


Figure 15. Histograms of the number distributions of HCO^+ abundances for each evolutionary sequence. The name of the evolutionary stage is given on the top left corner of each panel. The vertical dashed lines indicate the median values of the abundances for each distribution. The diagonal patterns indicate the portions of the histograms that correspond to upper and lower limits (see bottom panel, right side). The median values and the K-S test suggest that abundances increase with the evolution of the clumps. Median values of the column densities are given in Table 8.

between each one of them and N_2H^+ , HCO^+ , or HNC show higher ratios in later stages of evolution. Because the number of SiO, HC_3N and HNC detections is low, the histograms with the number distributions of abundance ratios were not made. On the other hand, C_2H has a larger number of detections and shows no clear trends when abundance ratios are taken with respect to N_2H^+ , HCO^+ , or HNC.

4.3. Assumptions and limitations in calculating column densities and abundances

This section discusses the major assumptions and limitations that affect the calculations of column densities and molecular abundances. Although the assumptions used in this work are widely used in the literature, it is important to be aware of their implications.

Temperature. Under the assumption of local thermodynamic equilibrium (LTE) conditions, we assume that the excitation temperature for all molecules is identical to the dust temperature for a given source. This assumption is reasonable since the critical densities of the molecules that were used to calculate physical parameters (between $2 \times 10^5 - 2 \times 10^6 \text{ cm}^{-3}$) are comparable to the density of the sources ($\sim 10^6 \text{ cm}^{-3}$; Rathborne et al. 2010), implying they are close to thermalization. However, the dust temperature is an average temperature along the line of sight, and may not necessarily reflect the temperature of the dust and gas in the portion of the clumps/cores which are dense enough to produce the emission lines we are observing. We note that the molecular abundance ratios ($\text{N}_2\text{H}^+/\text{HCO}^+$ and $\text{N}_2\text{H}^+/\text{HNC}$) are practically independent of temperature because of a similar dependence on temperature for the individual abundances. The abundance ratio for a given source at 15 and 50 K varies only $\sim 0.4\%$.

Isotopic abundance ratio. In the calculation of optical depths and column densities for HCO^+ and HNC,

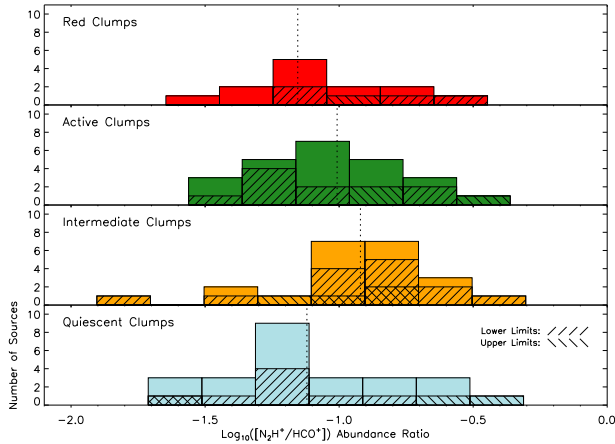


Figure 16. Histograms of the number distributions of $\text{N}_2\text{H}^+/\text{HCO}^+$ abundance ratios for each evolutionary sequence. The name of the evolutionary stage is given on the top left corner of each panel. The vertical dashed lines indicate the median values of the abundance ratios for each distribution. The diagonal patterns indicate the portions of the histograms that correspond to upper and lower limits (see bottom panel, right side). The median values and the K-S test suggest that $\text{N}_2\text{H}^+/\text{HCO}^+$ ratios act as a chemical clock, increasing their values with the evolution of the clumps, from intermediate, to active, to red clumps. It is not clear why this trend does not include quiescent clumps (see Section 4.2.2). Median values of the abundance ratios are given in Table 8.

we have assumed a constant value of 50 for the $^{12}\text{C}/^{13}\text{C}$ isotopic abundance ratio for all sources, regardless of their different distances to the Galactic center. However, it has been shown that there is a gradient of this ratio increasing outwards from the Galactic center (Savage et al. 2002). The $^{12}\text{C}/^{13}\text{C}$ ratio has been measured using several methods and ranges from ~ 20 to ~ 70 (Savage et al. 2002, and references therein). The variation of the $^{12}\text{C}/^{13}\text{C}$ ratio can give an error of a factor ~ 2 in the column density estimation.

Dust emission properties. H_2 column densities were calculated using the smoothed 1.2 mm emission data from Rathborne et al. (2006) and the same procedure that they used. The main assumptions are that the dust opacity per gram of gas, $\kappa_{1.2\text{mm}}$, is $1.0 \text{ cm}^2 \text{ g}^{-1}$, and the gas-to-dust mass ratio is 100. The value for $\kappa_{1.2\text{mm}}$ was determined by Ossenkopf & Henning (1994) for protostellar cores assuming dust grains with thin ice mantles at gas densities of 10^6 cm^{-3} . However, dust opacities and the gas-to-dust ratio are not well constrained. They could vary due to dust destruction in later stages of evolution (by shocks or UV radiation), or grain growth in dense, cold cores at very early stages. In the first scenario, the gas-to-dust ratio would be greater than 100; in the second scenario, the gas-to-dust ratio would be less than 100 and $\kappa_{1.2\text{mm}}$ would decrease.

4.4. Molecules

In this section, we discuss each commonly detected molecular line in depth. We describe the structure of the lines with hyperfine transitions (N_2H^+ , HCN, and C_2H), a brief review about their formation and previous works, and their behavior in IRDC clumps.

4.4.1. N_2H^+ (Diazenylium)

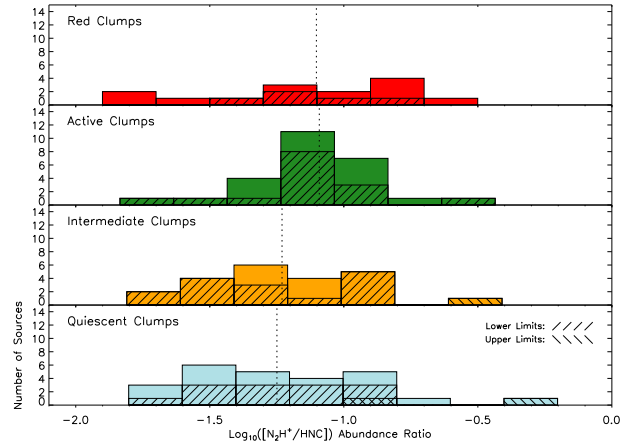


Figure 17. Histograms of the number distributions of $\text{N}_2\text{H}^+/\text{HNC}$ abundance ratios for each evolutionary sequence. The name of the evolutionary stage is given on the top left corner of each panel. The vertical dashed lines indicate the median values of the abundance ratios for each distribution. The diagonal patterns indicate the portions of the histograms that correspond to upper and lower limits (see bottom panel, right side). The median values and the K-S test suggest that the $\text{N}_2\text{H}^+/\text{HNC}$ ratio may act as chemical clock, increasing their median values with the evolution of the clumps, from quiescent to red clumps. Median values of the abundance ratios are given in Table 8.

The $\text{N}_2\text{H}^+ J = 1 \rightarrow 0$ rotational transition exhibits a quadrupole hyperfine structure due to the spin of the two nitrogen nuclei. Although for $\text{N}_2\text{H}^+ J = 1 \rightarrow 0$ there are 15 allowed hyperfine transitions (Daniel et al. 2006), only seven features can be resolved in low-mass star forming regions (e.g., Caselli et al. 1995; Crapsi et al. 2005) and three in high-mass star forming regions (e.g., Foster et al. 2011). In the latter case, because massive star-forming regions show turbulent line widths ($> 3 \text{ km s}^{-1}$) much broader than thermal widths ($\sim 0.3 \text{ km s}^{-1}$), two triplets are blended and observed as one line. The relative intensities in the optically thin case are given by the statistical weights 1:3:5:7, when seven components are detected, and 1:3:5, when three components are detected. The relative intensities become one in the optically thick case.

N_2H^+ is a good tracer of dense, cold gas because it does not deplete at low temperatures and high densities. Because the N_2H^+ spectrum show no evidence of self-absorbed profiles or line wings indicating outflow activity, this molecule is also a good tracer of dense, warm gas. However, some clumps have broad lines, which may suggest they are formed by more than one central object. Indeed, high angular resolution observations made with interferometers show the clumpy nature of IRDCs (e.g., Rathborne et al. 2007, 2008; Zhang et al. 2009). N_2H^+ is the second most frequently detected line in this survey and its detection rates do not depend of the star formation activity. However, the brightness temperature of N_2H^+ is normally weak in regions without signs of star formation. N_2H^+ column densities and abundances increase with the evolution of the clumps. Although, in general, an increase of column density does not necessarily mean an increase of the molecular abundance, we see in our sample of objects that column density and abundance of N_2H^+ tend to increase together. The increase of column density with the evolution of the clumps

might be explained by the accretion of material. For instance, Chambers et al. (2009) showed that, on average, clumps with signs of star formation have smaller sizes and higher densities than clumps without apparent star formation and Zhang & Wang (2011) propose that embedded protostars and protostellar cores undergo simultaneous mass growth during the protostellar evolution. The increase in the abundance might be explained by the rise in the temperature which releases N_2 from the dust grains to the gas phase allowing the formation of more N_2H^+ with the passage of time. However, with the increase of temperature, CO should also be released from the dust grains into the gas phase and should efficiently destroy N_2H^+ (Lee et al. 2004; Jørgensen et al. 2004; Busquet et al. 2011). Why exactly N_2H^+ abundance increases with evolution is not clear. We suggest two possible explanations. First, the rates involving the formation and destruction of N_2 , CO, N_2H^+ , and HCO^+ might not be accurate, and N_2H^+ might not be destroyed as efficiently as is currently believed. Second, the large beam of Mopra is including emission from cold gas which is surrounding the most compact regions directly associated with the star formation processes in the center of the clumps. If most of the N_2H^+ emission is coming from a cold envelope, in clumps that show signs of star formation, we are using in the abundance calculation a higher temperature than the actual value. Higher temperatures would lead us to infer larger N_2H^+ abundances. Busquet et al. (2011) performed a time-dependent chemical modeling of the massive protostellar cluster AFGL5142 based on the model of Viti et al. (2004). Their model consists of a prestellar and a protostellar phase. From their Figure 9, it can be seen that

once temperature increases, from the prestellar to the protostellar phase, the N_2H^+ molecular abundance also increases, supporting what we see in our work.

4.4.2. HCO^+ and $H^{13}CO^+$ (Formylionium)

HCO^+ has been widely used to investigate infall motions (e.g., Fuller et al. 2005; Chen et al. 2010), and, occasionally, its spectrum shows high-velocity wing emission which indicates outflow activity (e.g., Cyganowski et al. 2011). This makes HCO^+ a good tracer of kinematics in star-forming regions. On the other hand, $H^{13}CO^+$ is optically thin and normally shows a Gaussian profile. The combination of these two lines is usually used to distinguish between an asymmetric “blue profile” (indicative of infall motions) and two velocity components in the line of sight. If the optically thin $H^{13}CO^+$ peaks in the self-absorption of the optically thick HCO^+ , it indicates a genuine “blue profile.” In our sample of IRDC clumps, three intermediate clumps (G024.33 MM2, G024.33 MM5, and G031.97 MM5) present this characteristic profile associated with large-scale infall motions. As also happens for N_2H^+ , HCO^+ column densities and abundances rise with the evolution of the clumps. As we mentioned before for N_2H^+ , the increase in HCO^+ column densities might be due to the physical evolution of the clumps. The rise in HCO^+ abundance can be plausibly explained by the increase in the temperature, which releases CO from grain mantles into the gas phase, forming more HCO^+ with the passage of time. For example, although Busquet et al. (2011) focused on the NH_3/N_2H^+ abundance ratio, they also obtained HCO^+ abundances from their chemical modeling. They showed that once temperature rises, from the prestellar to the protostellar phase, the HCO^+ molecular abundance rises, as well as that of N_2H^+ .

Table 8
Median Values of Derived Clump Properties for each Evolutionary Stage

Molecule	Quiescent Clumps	Intermediate Clumps	Active Clumps	Red Clumps	All Clumps
Optical Depths (τ)					
HNC	24	22	18	16	19
N_2H^+ ^a	0.8	0.8	0.5	1.8	0.8
HCO^+	30	20	16	19	21
C_2H^b	2.9	2.4	2.2	1.4	2.4
Column Densities (cm^{-2})					
HNC	1.84×10^{14}	2.50×10^{14}	3.39×10^{14}	2.45×10^{14}	2.42×10^{14}
N_2H^+	1.03×10^{13}	1.40×10^{13}	2.34×10^{13}	2.75×10^{13}	1.60×10^{13}
HCO^+	1.40×10^{14}	1.51×10^{14}	2.51×10^{14}	3.20×10^{14}	1.88×10^{14}
C_2H	2.02×10^{14}	2.40×10^{14}	2.66×10^{14}	2.68×10^{14}	2.41×10^{14}
HC_3N	3.05×10^{12}	4.10×10^{12}	5.47×10^{12}	7.97×10^{12}	4.77×10^{12}
HNCO	1.33×10^{13}	3.36×10^{13}	4.30×10^{13}	4.31×10^{13}	3.36×10^{13}
SiO	1.36×10^{12}	...	1.39×10^{13}	4.62×10^{12}	7.72×10^{12}
Molecular Abundances					
HNC	3.52×10^{-8}	4.41×10^{-8}	3.29×10^{-8}	6.11×10^{-8}	3.73×10^{-8}
N_2H^+	1.65×10^{-9}	2.73×10^{-9}	3.13×10^{-9}	3.73×10^{-9}	2.40×10^{-9}
HCO^+	2.40×10^{-8}	2.48×10^{-8}	4.23×10^{-8}	5.65×10^{-8}	2.51×10^{-8}
C_2H	3.65×10^{-8}	3.45×10^{-8}	4.26×10^{-8}	4.92×10^{-8}	3.72×10^{-8}
HC_3N	3.14×10^{-10}	2.34×10^{-10}	4.97×10^{-10}	4.23×10^{-10}	4.23×10^{-10}
HNCO	1.83×10^{-9}	3.21×10^{-9}	2.51×10^{-9}	4.00×10^{-9}	2.80×10^{-9}
SiO	2.78×10^{-10}	...	5.95×10^{-10}	4.37×10^{-10}	5.79×10^{-10}
Abundance Ratios					
N_2H^+/HCO^+	0.08	0.12	0.10	0.07	0.09
N_2H^+/HNC	0.06	0.06	0.08	0.08	0.07

^a Optical depth for the brightest transition $JF_1F = 123 \rightarrow 012$.

^b Optical depth for the brightest transition $NJF = 1 \frac{3}{2} 2 \rightarrow 0 \frac{1}{2} 1$.

Table 9
Column Density Comparison with Other Works.

Different Works	N_2H^+ ($\times 10^{13}$) (cm^{-2})	HCO^+ ($\times 10^{14}$) (cm^{-2})	HNC ($\times 10^{14}$) (cm^{-2})	C_2H ($\times 10^{14}$) (cm^{-2})	HC_3N ($\times 10^{12}$) (cm^{-2})	HNC O ($\times 10^{13}$) (cm^{-2})	SiO ($\times 10^{13}$) (cm^{-2})
This Work	Q: 1.03 A: 2.34	A: 2.51 R: 3.20	A: 3.39 ...	A: 2.66 ...	Q: 3.05 ...	A: 4.30 R: 4.31	A: 1.39 R: 0.46
Sakai et al. (2008)	Q: 1.15	Q: 9.70
Pirogov et al. (2003)	A: 2.78
Sakai et al. (2010)	...	A: 3.30	A: 3.60	A: 3.25	A: 1.46
Purcell et al. (2006)	...	R: 11.7
Zinchenko et al. (2000)	A-R: 8.61	...
Miettinen et al. (2006)	R: 2.00

Note. — Q = Quiescent; A = Active; R = Red.
This table displays median values for comparison.

4.4.3. HNC and HN^{13}C (*Hydrogen Isocyanide*)

HNC is the molecule with the highest detection rate in the sample and its presence is independent of the star formation activity. Because HNC is ubiquitous in the IRDC clumps, and its spectrum shows no evidence of line wings indicating outflows and only a few self-absorbed profiles, HNC seems to be a good tracer of cold and warm gas. The HNC emission lines show, in general, broad widths (as seen in the HCO^+ lines as well, Figure 9). This is probably because both lines are optically thick, and ΔV can be broader by opacity. On the other hand, HN^{13}C is optically thin and normally shows a Gaussian profile. We note that the assumption of HNC emission being optically thin produces column densities of at least one order of magnitude lower. There is a slight increase of HNC column densities with the evolution of the clumps. However, there are no differences in the HNC abundances for the different evolutionary states. The accretion of material in the star-forming clumps could explain the small rise in the HNC column densities. From the histogram with the relative abundances of N_2H^+ and HNC (Figure 17), it can be inferred that HNC may be preferentially formed in cold gas. Future chemical modeling is needed to clarify the behavior of HNC in high-mass star-forming regions.

4.4.4. HCN (*Hydrogen Cyanide*)

The $\text{HCN } J = 1 \rightarrow 0$ rotational transitions show three hyperfine components caused by the nuclear spin of the nitrogen nucleus. In the optically thin case, these three components have relative intensities of 1:3:5. However, due to the broad linewidths found in massive star-forming regions, the components are blended. In addition, several sources exhibit spectra with extended wing emission and a wide variety of relative intensities other than those in the optically thin limit. The combination of these three factors makes it difficult to perform Gaussian fits and analyze the HCN line towards the IRDC clumps in this survey. For a better understanding of HCN hyperfine transitions, see the recent work of Loughane et al. (2012).

4.4.5. C_2H (*Ethynyl*)

$\text{C}_2\text{H } N = 1 \rightarrow 0$ exhibits 6 fine and hyperfine components due to the presence of both an electron spin and

a nuclear spin of the hydrogen nucleus. The spectral separation makes all of them observable in star-forming regions. However, two of them are relatively very weak and were not detected in this survey. Their relative intensities in the optically thin case are given by Tucker et al. (1974) and Padovani et al. (2009).

C_2H has been known to be a PDR tracer (e.g., Fuente et al. 1993). However, Beuther et al. (2008) find that this molecule also seems to trace dense gas in early stages of star formation. They found that the distribution of C_2H shows a hole around a hot core, and suggest that C_2H decreases in the hot core phase. Based on the results of their simple chemical modeling, they suggest that C_2H may be a suitable tracer of early stages of star formation.

So far, C_2H has not been systematically studied in massive star-forming regions or IRDCs. Although we cannot know the spatial distribution of C_2H in the IRDC clumps, we can say that there is definitely an increase in C_2H detections from quiescent to active sources (see Figure 7). The $\sim 30\%$ detection rate of this line in quiescent clumps shows that its emission is not ubiquitous in these kinds of sources as, for example, N_2H^+ , HNC , and HCO^+ are. Certainly, higher angular resolution observations and mapping are needed to clarify if the C_2H emission comes from the external layers of clumps that can interact with PDR emission surrounding them, or if the C_2H emission comes from the dense, cold gas inside quiescent clumps. We note that C_2H lines show the best ΔV correlation with N_2H^+ , suggesting that the emission originates from the same region (see Figure 9). C_2H column densities and abundances show no clear trend of changing with evolution. There is marginal evidence for increasing column densities with the evolution of the clumps, but it is not supported by the K-S test.

4.4.6. HC_3N (*Cyanoacetylene*)

HC_3N is the simplest of the cyanopolynes, molecules in the form of HC_{2n+1}N with n from 1 to 5. Its main progenitor, C_2H_2 , exists on grains mantles and is released into the gas phase during the onset of heating. Thus, HC_3N is associated with warm, dense gas in regions with current star formation, such as hot cores (e.g., Chapman et al. 2009). This may explain the high detection rates ($\sim 50\%$) for this molecule in active clumps. The presence of HC_3N and the rich molecular line spectra found in active cores (see Figure 6), suggest that some active clumps may have embedded hot molecular

cores, as, for example, Rathborne et al. (2008) found in one IRDC clump using high angular resolution observations. The HC_3N linewidths are more narrow than N_2H^+ linewidths, and seem to correlate better with those of

H^{13}CO^+ and HN^{13}C (see Figure 9). HC_3N column densities vary with the evolution of the clumps, increasing in more evolved regions as is shown by the median values. For HC_3N abundances, no real change is clear.

Table 10
Continuum Emission Parameters and Molecular Abundances

IRDC Clump	1.2 mm Flux (mJy)	$\text{N}(\text{H}_2) \times 10^{22} (\text{cm}^{-2})$	Molecular Abundance						
			$\text{N}_2\text{H}^+ \times 10^{-9}$	$\text{HCO}^+ \times 10^{-8}$	$\text{HNC} \times 10^{-8}$	$\text{C}_2\text{H} \times 10^{-8}$	$\text{HC}_3\text{N} \times 10^{-10}$	$\text{HNCO} \times 10^{-9}$	$\text{SiO} \times 10^{-10}$
G015.05 MM1	45	0.86	1.82(0.15)	2.39(0.85)	2.64(1.27)	3.20(3.52)	...	1.94(0.81)	...
G015.05 MM2	25	0.35	2.05(0.45)	1.69(0.60)	7.70(5.53)
G015.05 MM3	18	0.33	1.08(0.31)	...	3.12(1.52)
G015.05 MM4	14	0.18	5.51(0.63)	3.09(1.07)	8.26(3.43)	16.20(17.41)
G015.05 MM5	24	0.32	1.63(0.51)	3.16(1.74)	7.50(4.84)
G015.31 MM2	22	0.43	2.73(2.89)	...	5.05(4.12)
G015.31 MM3	17	0.32	0.96(0.25)	2.65(1.90)	1.58(1.61)
G015.31 MM5	22	0.34	...	3.22(1.83)	3.98(2.79)
G018.82 MM2	77	0.82	2.74(2.75)	3.91(2.38)	4.21(2.55)
G018.82 MM3	30	0.36	16.75(16.99)	27.86(14.46)	18.52(8.67)
G018.82 MM4	43	1.26	0.85(0.14)	6.73(5.33)	3.98(2.25)	0.77(0.83)	...
G018.82 MM6	46	0.88	1.39(0.14)	0.60(0.21)	0.91(0.40)
G019.27 MM2	46	0.65	3.36(0.22)	...	6.30(2.15)	6.40(7.08)
G022.35 MM1	93	2.19	0.19(0.05)	0.39(0.15)	0.51(0.21)
G022.35 MM2	32	0.29	6.94(3.70)
G023.60 MM7	49	0.43	9.45(9.31)	...	8.00(3.82)
G023.60 MM9	32	0.41	1.67(0.27)	...	3.58(1.72)	3.68(5.28)
G024.08 MM2	48	0.72	0.98(0.16)	2.49(1.01)	3.52(1.57)
G024.08 MM3	33	0.48	1.94(1.92)	3.72(1.85)	3.98(1.77)
G024.08 MM4	45	0.63	0.76(0.21)	3.86(3.50)	2.92(1.49)
G024.33 MM2	44	0.56	5.44(0.32)	2.43(0.63)	10.94(2.07)	7.58(1.95)	...
G024.33 MM3	53	0.70	3.77(0.24)	1.97(0.50)	1.22(0.41)	4.85(6.65)	...	4.01(1.28)	5.64(2.02)
G024.33 MM4	53	0.72	2.19(0.19)	1.10(0.42)	1.10(0.40)
G024.33 MM5	51	0.67	3.24(0.22)	4.18(0.68)	1.18(0.42)	3.92(5.95)	...	8.10(1.39)	...
G024.33 MM7	26	0.49	1.89(0.17)	2.49(0.47)	2.15(0.78)	1.24(2.46)	2.78(1.51)
G024.33 MM8	42	0.55	...	2.50(0.95)	4.69(1.80)
G024.33 MM9	43	0.31	...	7.24(2.81)	10.96(4.29)
G024.33 MM11	32	0.55	2.76(0.17)	5.16(1.14)	7.34(2.73)
G024.60 MM2	78	1.54	0.81(0.06)	0.98(0.32)	0.96(0.41)	0.75(0.26)	2.25(0.80)
G025.04 MM2	59	0.91	0.68(0.12)	1.39(0.56)	1.87(0.80)
G025.04 MM4	62	0.89	2.74(0.12)	1.69(0.61)	4.82(1.13)	1.22(2.49)	...	3.50(0.73)	...
G027.75 MM2	17	0.32	3.12(3.15)
G027.94 MM1	41	0.37	4.44(4.46)	...	5.28(1.83)	5.19(8.39)
G028.04 MM1	44	0.47	4.87(4.79)	4.80(2.04)	11.79(5.69)	2.73(4.87)	8.07(2.62)	6.17(1.80)	...
G028.08 MM1	29	0.61	1.03(1.02)	...	3.14(1.66)
G028.23 MM1	59	1.23	2.54(2.55)	0.81(0.27)	0.62(0.22)
G028.28 MM4	43	0.51	2.96(0.26)	3.55(0.73)	3.20(1.17)	5.19(5.99)
G028.37 MM1	318	4.02	1.14(0.04)	0.62(0.10)	1.42(0.24)	1.07(0.60)	3.60(0.36)	2.48(0.22)	3.98(0.34)
G028.37 MM2	118	1.23	2.04(0.15)	1.97(0.36)	5.18(1.43)	3.70(5.25)	3.96(1.73)	2.94(1.22)	...
G028.37 MM4	115	1.51	3.10(0.12)	1.92(0.20)	2.89(0.31)	4.17(3.73)	5.65(0.71)	5.33(0.42)	9.20(0.65)
G028.37 MM6	87	1.71	1.56(0.06)	1.59(0.30)	1.68(0.27)	1.06(1.38)	4.48(0.71)	2.51(0.30)	5.96(0.52)
G028.37 MM9	67	1.21	1.26(0.09)	1.64(0.29)	1.26(0.24)
G028.37 MM11	53	0.60	1.74(0.34)	1.36(0.47)	11.93(6.30)	4.36(6.98)
G028.37 MM12	51	0.97	0.92(0.93)	2.49(1.42)	3.71(2.94)	...	3.14(1.58)
G028.37 MM13	20	0.28	5.16(5.59)
G028.53 MM3	85	1.78	1.39(1.37)	1.19(0.36)	1.34(0.58)
G028.53 MM5	44	0.63	4.63(4.83)	2.39(1.62)	5.48(3.21)
G028.53 MM7	44	0.86	1.28(0.14)	1.06(0.31)	4.03(1.41)
G028.53 MM8	35	0.54	1.84(0.26)	6.53(5.13)	6.35(3.27)	3.73(2.12)
G028.53 MM9	61	0.94	2.00(0.16)	2.53(1.01)	3.27(1.07)
G028.53 MM10	90	1.28	1.59(0.15)	2.22(0.85)	3.83(1.14)	3.96(5.40)
G028.67 MM1	27	0.27	...	6.07(3.02)	10.93(5.20)
G028.67 MM2	38	0.76	0.95(0.14)	...	3.51(2.09)
G030.14 MM1	40	0.64	2.12(2.33)	1.83(1.05)	2.50(1.28)
G030.57 MM1	117	1.40	3.16(0.11)	...	2.75(0.87)	1.89(2.95)	6.10(1.11)	2.04(0.70)	...
G030.57 MM3	17	0.34	2.92(0.55)	...	18.84(10.70)	7.12(10.94)
G030.97 MM1	98	1.08	3.38(0.14)	4.80(0.46)	3.75(0.62)	...	3.43(1.13)
G031.97 MM5	29	0.35	6.77(0.39)	3.63(0.85)	10.27(3.34)	8.52(11.04)
G031.97 MM7	36	0.59	2.89(0.16)	2.05(0.40)	5.13(4.79)	3.66(5.80)	...	1.70(0.96)	...
G031.97 MM8	38	0.31	10.84(0.62)	...	10.76(3.73)
G033.69 MM1	97	1.71	2.08(0.06)	1.00(0.15)	1.72(0.20)	...	5.61(0.75)	2.66(0.35)	3.09(0.60)
G033.69 MM2	75	0.73	4.34(0.29)	6.17(2.51)	6.11(1.56)	4.84(0.67)	13.77(2.24)	5.87(1.66)	...
G033.69 MM3	52	0.48	4.97(0.58)	7.48(3.12)	10.73(4.33)
G033.69 MM4	65	1.00	3.06(0.21)	1.77(0.65)	3.38(0.83)	...	5.59(1.97)	3.09(1.02)	...
G033.69 MM5	44	0.49	4.42(0.50)	7.90(3.93)	8.69(3.61)	7.70(6.26)

Table 10 — *Continued*

IRDC Clump	1.2 mm Flux (mJy)	N(H ₂) ×10 ²² (cm ⁻²)	Molecular Abundance						
			N ₂ H ⁺ ×10 ⁻⁹	HCO ⁺ ×10 ⁻⁸	HNC ×10 ⁻⁸	C ₂ H ×10 ⁻⁸	HC ₃ N ×10 ⁻¹⁰	HNCO ×10 ⁻⁹	SiO ×10 ⁻¹⁰
G033.69 MM11	37	0.65	...	3.88(1.46)	6.14(2.33)	2.28(4.42)
G034.43 MM1	548	5.85	2.34(0.04)	0.82(0.09)	2.33(0.27)	1.32(0.81)	5.70(0.36)	1.47(0.25)	5.94(0.36)
G034.43 MM5	89	1.75	1.70(0.05)	1.10(0.15)	2.99(0.45)	...	3.07(0.71)
G034.43 MM7	59	0.85	1.31(0.12)	1.26(0.39)	2.69(0.70)	2.41(3.42)	2.43(1.38)
G034.43 MM8	69	0.64	2.39(0.26)	4.23(1.89)	3.98(1.58)	5.56(9.33)
G034.77 MM1	111	1.11	3.68(3.65)	4.08(0.71)	2.20(0.72)	...	4.21(1.17)
G034.77 MM3	18	0.25	3.55(0.60)	2.03(0.71)	11.20(4.72)	12.12(20.78)
G035.39 MM7	50	0.61	3.92(0.27)	9.77(1.54)	6.21(1.34)	7.13(6.73)	5.27(2.41)
G035.59 MM1	22	0.25	11.25(12.28)	17.36(8.70)	7.02(4.36)
G035.59 MM2	19	0.35	2.03(0.29)	5.09(1.59)	3.05(1.14)
G035.59 MM3	30	0.42	2.40(0.55)	2.69(0.70)	3.00(1.13)	4.37(5.26)	3.32(2.99)
G036.67 MM1	38	0.90	1.10(1.13)	1.75(1.49)	1.13(0.66)	1.75(1.74)
G036.67 MM2	38	1.22	...	0.54(0.24)	0.95(0.39)
G038.95 MM1	104	3.33	0.40(0.02)	1.28(0.20)	0.51(0.15)	0.72(0.58)	1.41(0.58)	0.27(0.16)	...
G038.95 MM2	82	0.82	2.10(0.25)	5.66(1.29)	2.99(1.12)	...	4.23(2.10)
G038.95 MM3	57	0.88	3.40(3.38)	3.88(1.00)	2.69(1.06)	3.20(0.46)
G038.95 MM4	44	0.40	4.89(4.95)	4.54(1.69)	5.81(2.28)	5.36(0.97)	6.16(4.48)
G053.11 MM1	227	2.43	1.28(0.10)	1.95(0.20)	0.81(0.24)	...	3.28(0.57)
G053.11 MM2	55	0.63	4.39(4.42)	4.47(0.90)	2.97(0.85)	2.58(0.98)
G053.11 MM4	34	0.34	3.29(0.50)	11.95(1.79)	4.29(1.14)	2.79(1.06)	4.69(3.59)
G053.11 MM5	25	0.22	13.32(13.61)	5.79(2.17)	7.07(2.69)	4.97(1.14)
G053.25 MM1	52	0.61	2.36(0.24)	2.28(0.75)	1.98(0.68)	2.54(3.40)
G053.25 MM3	17	0.20	6.87(7.23)	7.48(3.09)	6.77(2.63)	15.56(26.01)
G053.25 MM4	37	0.40	3.99(0.37)	6.01(1.37)	3.04(1.07)
G053.25 MM5	17	0.20	...	12.49(4.32)	6.76(2.55)	10.04(22.70)
G053.25 MM6	34	0.30	13.05(13.20)	8.97(2.12)	5.61(2.10)
G053.31 MM2	34	0.59	2.09(2.07)	1.13(0.42)	1.69(0.65)

4.4.7. HNCO (*Isocyanic Acid*)

HNCO is a high density tracer that has been found in regions that span a large range of temperatures (10-500 K; Jackson et al. 1984; Zinchenko et al. 2000; Bisschop et al. 2007). The formation of HNCO is inefficient if only gas-phase reactions are considered (Tideswell et al. 2010). In hot cores, the gas formation chemistry can explain the observed HNCO abundances when reactions on the surfaces of grains are included. HNCO is efficiently formed on grain mantles and processed in more complex molecules. However, HNCO is not directly ejected from the dust. Instead, it is formed by the dissociation of more complex molecules (formed by HNCO on the grain mantles) once they are released to the gas phase (Tideswell et al. 2010; Rodríguez-Fernández et al. 2010). Zinchenko et al. (2000) found evidence that HNCO and SiO may have a common production mechanism, presumably based on shock chemistry. Rodríguez-Fernández et al. (2010) found HNCO lines that exhibit the same characteristics as other well-known shock tracers such as CH₃OH and some sulfur-bearing species (SO and SO₂). These authors suggest that HNCO is a shock tracer which is explained by a combination of grain surface and gas phase chemistry. HNCO abundances would rise in shock regions because this molecule can be directly ejected to the gas phase through grain sputtering and because the efficiency of neutral-neutral reactions increases in the gas phase due to higher gas temperatures.

In our IRDC sample, HNCO emission is detected slightly more often in regions with signs of star forma-

tion. The HNCO line widths seem to correlate with those of N₂H⁺. HNCO profiles show no evident signatures of being a tracer of shocks in most of the sources, except in G028.37 MM1 and G028.37 MM4 (which represent 10% of the sources with HNCO detection). In these two sources, the HNCO spectrum presents a blue wing which is also observed in SiO. HNCO column densities rise with the evolution of the clumps, as is shown by the median values. However, HNCO abundances do not show this trend.

4.4.8. SiO (*Silicon Monoxide*)

It is well-known that SiO is a powerful tracer of molecular gas associated with shocks (Schilke et al. 1997; Caselli et al. 1997). Its abundance is highly enhanced in molecular outflows, with respect to the ambient abundances. In some cases these enhancements can be up to 10⁶ (Martin-Pintado et al. 1992). The increase of the SiO abundance is due to the silicate grain destruction, giving rise to the injection into gas of Si atoms and/or Si-bearing species, and the subsequent high temperature gas-phase chemistry (Schilke et al. 1997; Caselli et al. 1997). The previous SiO production mechanism explains spectral lines that show extended wing emission with broad line widths caused by the interaction of outflows and the surrounding medium. However, an SiO component coming from quiescent gas is not well understood. Jiménez-Serra et al. (2010) detected extended narrow SiO emission not associated with signs of star formation in an IRDC. They suggest that this SiO component could be produced by the following processes: remnants of large-scale shocks caused by the formation process of the IRDC, decelerated shocked gas associated with large scale outflows from neighboring massive

protostars, recently processed material associated with the youngest jets/outflows, and/or an undetected and widespread lower mass protostar population.

In our IRDC sample, SiO emission is mostly detected in clumps with signs of star formation. The only exception is the quiescent clump G024.33 MM7 which shows a narrow line profile (1.4 km s^{-1}) and the lowest SiO abundance in the sample. The average SiO line width in the sample is $\sim 5 \text{ km s}^{-1}$. Half of the sources with SiO detection show clear extended wing emission indicating the presence of outflow activity.

5. CONCLUSIONS

We have carried out a multi-line survey at 3 mm toward 37 IRDCs, containing 159 clumps, in order to investigate the behavior of the different molecular tracers and search for chemical variations through an evolutionary sequence based on *Spitzer* IRAC and MIPS emission. We observed N_2H^+ , HNC, HN^{13}C , HCO^+ , H^{13}CO^+ , HCN, C_2H , HC_3N , HNC, and SiO lines with the Mopra 22 m telescope located in Australia. After eliminating clumps that are not located in IRDCs and pairs of clumps that are placed within one Mopra beam, we base our study on 92 sources.

HNC and N_2H^+ lines are detected in almost every IRDC clumps at every evolutionary stage, indicating that their presence does not depend on the star formation activity. On the other hand, HC_3N , HNC, and SiO lines are predominantly detected in later stages of evolution, as expected from their formation paths.

The line widths of N_2H^+ slightly increase with the evolution of the clumps, which is likely produced by the rise of turbulence due to the enhancement of the star formation activity at later evolutionary stages. The increase is modest because, due to the large Mopra beam, we are also tracing the bulk motions of the gas, instead of just the densest regions associated with star formation.

Optical depth calculations show that the N_2H^+ line is mostly optically thin (median of 0.8) and the C_2H line is moderately optically thick (median of 2.4). HCO^+ and HNC lines are optically thick (medians of 21 and 19, respectively), while their isotopologues are optically thin (median of 0.4 for both). N_2H^+ opacities show no variations with the evolution of the clumps, whereas C_2H , HCO^+ and HNC show a slight decrease with the rise of star formation activity.

In general, column densities of the different molecules change for the different evolutionary stages defined by Chambers et al. (2009) and increase with the evolution of the clumps, with the exception of C_2H . However, this is not generally true for molecular abundances (i.e., after dividing by the total H_2 column density inferred from 1.2 mm continuum emission). Only the increases of N_2H^+ and HCO^+ abundances are statistically significant and reflect chemical evolution. This is consistent with the results of Busquet et al. (2011), who included both molecules in their chemical modeling of a massive star-forming region. Although it is expected a rise of the HCO^+ abundance with the evolution of the clumps, it is not clear why N_2H^+ also follows this trend.

The $\text{N}_2\text{H}^+/\text{HCO}^+$ abundance ratio acts as a chemical clock, increasing its value from intermediate to active and red clumps. This observed trend is consistent with the theoretical predictions. The chemical models

suggest that when clumps warm up, they release CO from grain mantles to the gas phase. This rise of CO increases the amount of HCO^+ , because CO is its main supplier, with respect to N_2H^+ , because CO is its main destroyer. However, the observed trend does not extend to quiescent clumps. This could be due to observational limitations or because the theoretical predictions are incorrect at very early stages of evolution. We also find that the $\text{N}_2\text{H}^+/\text{HNC}$ abundance ratio increases with the evolution of the clumps, from quiescent to red clumps. It is not clear why this ratio behaves in this way, but it suggests that HNC may be preferentially formed in cold gas.

J.M.J. gratefully acknowledges funding support from NSF Grant No. AST-0808001. G.G. acknowledges support from CONICYT projects FONDAF No. 15010003 and BASAL PFB-06. We also thank the anonymous referee for helpful comments.

REFERENCES

- Battersby, C., Bally, J., Jackson, J. M., et al. 2010, *ApJ*, 721, 222
 Beltrán, M. T., Cesaroni, R., Neri, R., et al. 2005, *A&A*, 435, 901
 Beuther, H., & Sridharan, T. K. 2007, *ApJ*, 668, 348
 Beuther, H., Semenov, D., Henning, T., & Linz, H. 2008, *ApJ*, 675, L33
 Bisschop, S. E., Jørgensen, J. K., van Dishoeck, E. F., & de Wachter, E. B. M. 2007, *A&A*, 465, 913
 Blackman, G. L., Brown, R. D., Godfrey, P. D., & Gunn, H. I. 1976, *Nature*, 261, 395
 Blake, G. A., Sutton, E. C., Masson, C. R., & Phillips, T. G. 1987, *ApJ*, 315, 621
 Botschwina, P. 1984, *Chemical Physics Letters*, 107, 535
 Botschwina, P., Horn, M., Flugge, J., & Seeger, S. 1993, *J. Chem. Soc., Faraday Trans.*, 623, 2219
 Busquet, G., Estalella, R., Zhang, Q., et al. 2011, *A&A*, 525, A141
 Carey, S. J., Clark, F. O., Egan, M. P., et al. 1998, *ApJ*, 508, 721
 Carey, S. J., Feldman, P. A., Redman, R. O., et al. 2000, *ApJ*, 543, L157
 Caselli, P., Myers, P. C., & Thaddeus, P. 1995, *ApJ*, 455, L77
 Caselli, P., Hartquist, T. W., & Havnes, O. 1997, *A&A*, 322, 296
 Caselli, P., Benson, P. J., Myers, P. C., & Tafalla, M. 2002, *ApJ*, 572, 238
 Chambers, E. T., Jackson, J. M., Rathborne, J. M., & Simon, R. 2009, *ApJS*, 181, 360
 Chapman, J. F., Millar, T. J., Wardle, M., Burton, M. G., & Walsh, A. J. 2009, *MNRAS*, 394, 221
 Chen, X., Shen, Z.-Q., Li, J.-J., Xu, Y., & He, J.-H. 2010, *ApJ*, 710, 150
 Chen, H.-R., Liu, S.-Y., Su, Y.-N., & Wang, M.-Y. 2011, *ApJ*, 743, 196
 Clemens, D. P. 1985, *ApJ*, 295, 422
 Crapsi, A., Caselli, P., Walmsley, C. M., Myers, P. C., Tafalla, M., Lee, C. W., & Bourke, T. L. 2005, *ApJ*, 619, 379
 Cyganowski, C. J., Whitney, B. A., Holden, E., et al. 2008, *AJ*, 136, 2391
 Cyganowski, C. J., Brogan, C. L., Hunter, T. R., Churchwell, E., & Zhang, Q. 2011, *ApJ*, 729, 124
 Daniel, F., Cernicharo, J., & Dubernet, M.-L. 2006, *ApJ*, 648, 461
 Devine, K. E., Chandler, C. J., Brogan, C., et al. 2011, *ApJ*, 733, 44
 Egan, M. P., Shipman, R. F., Price, S. D., et al. 1998, *ApJ*, 494, L199
 Emprechtinger, M., Caselli, P., Volgenau, N. H., Stutzki, J., & Wiedner, M. C. 2009, *A&A*, 493, 89
 Faúndez, S., Bronfman, L., Garay, G., et al. 2004, *A&A*, 426, 97
 Fontani, F., Palau, A., Caselli, P., et al. 2011, *A&A*, 529, L7
 Foster, J. B., Jackson, J. M., Barnes, P. J., et al. 2011, *ApJS*, 197, 25
 Fuente, A., Martín-Pintado, J., Cernicharo, J., & Bachiller, R. 1993, *A&A*, 276, 473

- Fuller, G. A., Williams, S. J., & Sridharan, T. K. 2005, *A&A*, 442, 949
- Garden, R. P., Hayashi, M., Hasegawa, T., Gatley, I., & Kaifu, N. 1991, *ApJ*, 374, 540
- Havenith, M., Zwart, E., Leo Meerts, W., & Ter Meulen, J. J. 1990, *J. Chem. Phys.*, 93, 8446
- Jackson, J. M., Armstrong, J. T., & Barrett, A. H. 1984, *ApJ*, 280, 608
- Jackson, J. M., Rathborne, J. M., Shah, R. Y., et al. 2006, *ApJS*, 163, 145
- Jackson, J. M., Finn, S. C., Rathborne, J. M., Chambers, E. T., & Simon, R. 2008, *ApJ*, 680, 349
- Jiménez-Serra, I., Caselli, P., Tan, J. C., et al. 2010, *MNRAS*, 406, 187
- Jørgensen, J. K., Schöier, F. L., & van Dishoeck, E. F. 2004, *A&A*, 416, 603
- Kauffmann, J., & Pillai, T. 2010, *ApJ*, 723, L7
- Kim, G., Lee, C. W., Kim, J., et al. 2010, *Journal of Korean Astronomical Society*, 43, 9
- Kim, S.-J., Kim, H.-D., Lee, Y., Minh, Y. C., Balasubramanyam, R., Burton, M. G., Millar, T. J., & Lee, D.-W. 2006, *ApJS*, 162, 161
- Lapinov, A. V., Golubiatnikov, G. Y., Markov, V. N., & Guarnieri, A. 2007, *Astronomy Letters*, 33, 121
- Lattanzi, V., Walters, A., Drouin, B. J., & Pearson, J. C. 2007, *ApJ*, 662, 771
- Lee, J.-E., Bergin, E. A., & Evans, N. J., II 2004, *ApJ*, 617, 360
- Lo, N., et al. 2009, *MNRAS*, 395, 1021
- Loughnane, R. M., Redman, M. P., Thompson, M. A., et al. 2012, *MNRAS*, 420, 1367
- Machin, L., & Roueff, E. 2006, *A&A*, 460, 953
- Markwardt, C. B. 2009, *Astronomical Data Analysis Software and Systems XVIII*, 411, 251
- Martin-Pintado, J., Bachiller, R., & Fuente, A. 1992, *A&A*, 254, 315
- Miettinen, O., Harju, J., Haikala, L. K., & Pomren, C. 2006, *A&A*, 460, 721
- Miettinen, O., Hennemann, M., & Linz, H. 2011, *A&A*, 534, A134
- Mollaaghababa, R., Gottlieb, C. A., Vrtilik, J. M., & Thaddeus, P. 1991, *ApJ*, 368, L19
- Müller, H. S. P., Thorwirth, S., Roth, D. A., & Winnewisser, G. 2001, *A&A*, 370, L49
- Müller, H. S. P., Schlöder, F., Stutzki, J., & Winnewisser, G. 2005, *Journal of Molecular Structure*, 742, 215
- Öberg, K. I., van Broekhuizen, F., Fraser, H. J., et al. 2005, *ApJ*, 621, L33
- Ossenkopf, V., & Henning, T. 1994, *A&A*, 291, 943
- Padovani, M., Walmsley, C. M., Tafalla, M., Galli, D., Müller, H. S. P. 2009, *A&A*, 505, 1199
- Pagani, L., Daniel, F., & Dubernet, M.-L. 2009, *A&A*, 494, 719
- Perault, M., Omont, A., Simon, G., et al. 1996, *A&A*, 315, L165
- Peretto, N., & Fuller, G. A. 2009, *A&A*, 505, 405
- Pillai, T., Wyrowski, F., Carey, S. J., & Menten, K. M. 2006, *A&A*, 450, 569
- Pillai, T., Kauffmann, J., Wyrowski, F., et al. 2011, *A&A*, 530, A118
- Pirogov, L., Zinchenko, I., Caselli, P., Johansson, L. E. B., & Myers, P. C. 2003, *A&A*, 405, 639
- Prasad, S. S., & Huntress, W. T., Jr. 1980, *ApJ*, 239, 151
- Purcell, C. R., et al. 2006, *MNRAS*, 367, 553
- Ragan, S. E., Bergin, E. A., & Wilner, D. 2011, *ApJ*, 736, 163
- Rathborne, J. M., Jackson, J. M., & Simon, R. 2006, *ApJ*, 641, 389
- Rathborne, J. M., Simon, R., & Jackson, J. M. 2007, *ApJ*, 662, 1082
- Rathborne, J. M., Jackson, J. M., Zhang, Q., & Simon, R. 2008, *ApJ*, 689, 1141
- Rathborne, J. M., Jackson, J. M., Chambers, E. T., Stojimirovic, I., Simon, R., Shipman, R., & Frieswijk, W. 2010, *ApJ*, 715, 310
- Raymonda, J. W., Muenter, J. S., & Klemperer, W. A. 1970, *J. Chem. Phys.*, 52, 3458
- Rodríguez-Fernández, N. J., Tafalla, M., Gueth, F., & Bachiller, R. 2010, *A&A*, 516, A98
- Rodríguez-Franco, A., Martin-Pintado, J., & Fuente, A. 1998, *A&A*, 329, 1097
- Rygl, K. L. J., Wyrowski, F., Schuller, F., & Menten, K. M. 2010, *A&A*, 515, A42
- Savage, C., Apponi, A. J., Ziurys, L. M., & Wyckoff, S. 2002, *ApJ*, 578, 211
- Sakai, T., Sakai, N., Kamegai, K., Hirota, T., Yamaguchi, N., Shiba, S., & Yamamoto, S. 2008, *ApJ*, 678, 1049
- Sakai, T., Sakai, N., Hirota, T., & Yamamoto, S. 2010, *ApJ*, 714, 1658
- Sakai, T., Sakai, N., Furuya, K., Aikawa, Y., Hirota, T., Yamamoto, S., 2012, *ApJ*, in press.
- Sanhueza, P., Garay, G., Bronfman, L., et al. 2010, *ApJ*, 715, 18
- Schilke, P., Walmsley, C. M., Pineau des Forets, G., & Flower, D. R. 1997, *A&A*, 321, 293
- Schöier, F. L., van der Tak, F. F. S., van Dishoeck, E. F., & Black, J. H. 2005, *A&A*, 432, 369
- Simon, R., Jackson, J. M., Rathborne, J. M., & Chambers, E. T. 2006, *ApJ*, 639, 227
- Simon, R., Rathborne, J. M., Shah, R. Y., Jackson, J. M., & Chambers, E. T. 2006, *ApJ*, 653, 1325
- Snyder, L. E., Hollis, J. M., & Watson, W. D. 1977, *ApJ*, 212, 79
- Thorwirth, S., Müller, H. S. P., & Winnewisser, G. 2000, *Journal of Molecular Spectroscopy*, 204, 133
- Tideswell, D. M., Fuller, G. A., Millar, T. J., & Markwick, A. J. 2010, *A&A*, 510, A85
- Tucker, K. D., Kutner, M. L., & Thaddeus, P. 1974, *ApJ*, 193, L115
- Turner, B. E., & Thaddeus, P. 1977, *ApJ*, 211, 755
- van der Tak, F. F. S., Müller, H. S. P., Harding, M. E., & Gauss, J. 2009, *A&A*, 507, 347
- Vasyunina, T., Linz, H., Henning, T., Zinchenko, I., Beuther, H., & Voronkov, M. 2011, *A&A*, 527, A88
- Viti, S., Collings, M. P., Dever, J. W., McCoustra, M. R. S., & Williams, D. A. 2004, *MNRAS*, 354, 1141
- Wang, Y., Zhang, Q., Rathborne, J. M., Jackson, J., & Wu, Y. 2006, *ApJ*, 651, L125
- Yamaguchi, Y., Richards, C. A., Jr., & Schaefer, H. F., III 1994, *J. Chem. Phys.*, 101, 8945
- Zhang, Q., Wang, Y., Pillai, T., & Rathborne, J. 2009, *ApJ*, 696, 268
- Zhang, Q., & Wang, K. 2011, *ApJ*, 733, 26
- Zinchenko, I., Henkel, C., & Mao, R. Q. 2000, *A&A*, 361, 1079